



# Heterochromatin establishment during early mammalian development is regulated by pericentromeric RNA and characterized by non-repressive H3K9me3

Adam Burton<sup>1</sup>, Vincent Brochard<sup>ID 2</sup>, Carmen Galan<sup>3,11</sup>, Elias R. Ruiz-Morales<sup>ID 1</sup>, Quirze Rovira<sup>ID 4</sup>, Diego Rodriguez-Terrones<sup>ID 1</sup>, Kai Kruse<sup>4</sup>, Stéphanie Le Gras<sup>5</sup>, Vishnu S. Udayakumar<sup>6</sup>, Hang Gyeong Chin<sup>6</sup>, André Eid<sup>ID 1,12</sup>, Xiaoyu Liu<sup>7</sup>, Chenfei Wang<sup>ID 7</sup>, Shaorong Gao<sup>ID 7</sup>, Sriharsa Pradhan<sup>6</sup>, Juan M. Vaquerizas<sup>ID 4,8</sup>, Nathalie Beaujean<sup>ID 2,9</sup>, Thomas Jenuwein<sup>3</sup> and Maria-Elena Torres-Padilla<sup>ID 1,10</sup>

**Following fertilization in mammals, the gametes are reprogrammed to create a totipotent zygote, a process that involves de novo establishment of chromatin domains. A major feature occurring during preimplantation development is the dramatic remodelling of constitutive heterochromatin, although the functional relevance of this is unknown. Here, we show that heterochromatin establishment relies on the stepwise expression and regulated activity of SUV39H enzymes. Enforcing precocious acquisition of constitutive heterochromatin results in compromised development and epigenetic reprogramming, which demonstrates that heterochromatin remodelling is essential for natural reprogramming at fertilization. We find that de novo H3K9 trimethylation (H3K9me3) in the paternal pronucleus after fertilization is catalysed by SUV39H2 and that pericentromeric RNAs inhibit SUV39H2 activity and reduce H3K9me3. De novo H3K9me3 is initially non-repressive for gene expression, but instead bookmarks promoters for compaction. Overall, we uncover the functional importance for the restricted transmission of constitutive heterochromatin during reprogramming and a non-repressive role for H3K9me3.**

The remodelling of histone modifications, particularly of heterochromatin after fertilization, is thought to be required for epigenetic reprogramming and the acquisition of totipotency. However, whether and how constitutive heterochromatin pathways regulate gene expression, chromatin structure and/or reprogramming in vivo in the early mammalian embryo remains elusive. Here, we set out to investigate the role of heterochromatin in the mouse embryo immediately after fertilization, specifically to address whether H3K9 trimethylation (H3K9me3) plays a regulatory role at the onset of development.

Mouse embryos start development with parental epigenetic asymmetry, whereby the maternal chromatin is enriched with constitutive heterochromatic histone modifications while the paternal genome is largely devoid of them<sup>1–3</sup>. Global levels of histone modifications associated with constitutive heterochromatin, such as H3K9me3, H3K64me3 and H4K20me3, sharply decrease after fertilization<sup>4–7</sup>. The SUV39H1 and SUV39H2 histone methyltransferases are key players in the catalysis of H3K9me3 at constitutive heterochromatin regions on the genome<sup>8–10</sup>. However, how heterochromatin is first established in mammals remains unknown.

## Results

**De novo H3K9me3 activity occurs immediately after fertilization.** The global decrease of H3K9me3 levels after fertilization is correlated with low levels of *Suv39h1* mRNA<sup>4,11</sup> (Fig. 1a), which is reflected in the absence of detectable SUV39H1 protein until the eight-cell stage (Fig. 1b; Extended Data Fig. 1a). However, when carefully examining H3K9me3 levels, we observed that while early zygotes immediately after fertilization displayed no detectable H3K9me3 in the paternal pronucleus, late zygotes showed a clear accumulation of H3K9me3 (Fig. 1c). This is in agreement with recent H3K9me3 data from chromatin immunoprecipitation followed by sequencing (ChIP-seq) experiments in mouse preimplantation embryos that showed acquisition of H3K9me3 in the paternal genome in zygotes<sup>12</sup>. Although a minor proportion of these regions are also detectable in sperm, which suggests that there is low level inheritance undetectable by immunofluorescence, these results were intriguing and indicate a previously unappreciated de novo H3K9 methylation activity in the first cell cycle after fertilization.

To determine which histone methyltransferase catalyses de novo H3K9 methylation, we first examined the expression of the second

<sup>1</sup>Institute of Epigenetics and Stem Cells, Helmholtz Zentrum München, München, Germany. <sup>2</sup>Université Paris-Saclay, INRAE, ENVA, BREED U1198, Jouy-en-Josas, France. <sup>3</sup>Department of Epigenetics, Max Planck Institute of Immunobiology and Epigenetics, Freiburg, Germany. <sup>4</sup>Max Planck Institute for Molecular Biomedicine, Münster, Germany. <sup>5</sup>Institut de Génétique et de Biologie Moléculaire et Cellulaire, CNRS/INSERM U964, CU de Strasbourg, France. <sup>6</sup>New England Biolabs, Ipswich, MA, USA. <sup>7</sup>Clinical and Translational Research Center of Shanghai First Maternity and Infant Hospital, School of Life Sciences and Technology, Tongji University, Shanghai, China. <sup>8</sup>MRC London Institute of Medical Sciences, Institute of Clinical Sciences, Faculty of Medicine, Imperial College London, London, UK. <sup>9</sup>Université Lyon 1, Inserm, Stem Cell and Brain Research Institute U1208, Bron, France. <sup>10</sup>Faculty of Biology, Ludwig Maximilians University, Munich, Germany. <sup>11</sup>Present address: Inmunología y Genética Aplicada, Madrid, Spain. <sup>12</sup>Present address: The Francis Crick Institute, London, UK. e-mail: [torres-padilla@helmholtz-muenchen.de](mailto:torres-padilla@helmholtz-muenchen.de)

*Suv39h* gene, *Suv39h2*, and results indicated that *Suv39h2* transcripts are abundant in oocytes and early embryos<sup>4,13,14</sup> (Fig. 1d). SUV39H2 protein showed a greater enrichment in the paternal pronucleus than the maternal pronucleus in late zygotes (Fig. 1e; Extended Data Fig. 1b,c), whereas SUV39H1 was undetectable in both pronuclei (Fig. 1b). However, we did not detect SUV39H2 in early zygotes (Extended Data Fig. 1d). Instead, SUV39H2 accumulation in the paternal pronucleus correlated with H3K9me3 appearance and persisted through the eight-cell stage (Fig. 1c,e). To address whether SUV39H2 is responsible for de novo H3K9me3, we performed RNA interference (RNAi) against *Suv39h2* in early zygotes (Fig. 1f; Extended Data Fig. 1e). *Suv39h2* RNAi led to a strong depletion of H3K9me3 in the paternal pronucleus compared with the controls (Fig. 1g,h). H3K9me3 levels continued to decrease in the two-cell stage after *Suv39h2* RNAi (Extended Data Fig. 1f,g), which suggests that changes in H3K9me3 are more dynamic than previously anticipated and is in agreement with recent data<sup>12</sup>. We did not observe changes in H3K9me3 levels on the maternal chromatin after *Suv39h2* RNAi, which suggests that there is either a localized reduction of H3K9me3 undetectable by this method or that a different methyltransferase may be responsible for the reported H3K9me3 acquisition here<sup>12</sup>. Thus, de novo H3K9me3 on the paternal chromatin is catalysed by SUV39H2. Moreover, SUV39H1 and SUV39H2 proteins display contrasting patterns of expression in early embryogenesis.

**Pericentromeric RNA modulates SUV39H2 activity and reduces H3K9me3 levels in zygotes.** The contrasting expression patterns of *Suv39h1* and *Suv39h2* prompted us to investigate potential biochemical differences between the two lysine methyltransferases (KMTs). The mouse SUV39H2—but not SUV39H1—harbours an extended amino-terminal domain<sup>14</sup> (Fig. 2a) that can bind RNA in vitro<sup>15</sup>. This basic domain provides an additional RNA affinity to SUV39H2, although both full-length SUV39H1 and full-length SUV39H2 can broadly interact with single-stranded and double-stranded nucleic acids<sup>16,17</sup>. This, along with previous research showing that pericentric H3K9me3 foci are dispersed after RNaseA treatment<sup>18</sup>, prompted us to investigate whether H3K9me3 is regulated by RNA in embryos. Because major satellite (MajSat) transcripts from the pericentromere are transcribed primarily from the paternal genome from both strands in zygotes<sup>4,19,20</sup> (Fig. 2b), we considered them as potential candidates for regulating SUV39H2 activity. We generated full-length recombinant SUV39H1 and SUV39H2 and incubated each of them with increasing MajSat double-stranded RNA (dsRNA) concentrations to allow for RNA binding, after which we performed KMT assays using histone H3.1 (Fig. 2c). SUV39H2 activity was attenuated with increasing

concentrations of dsRNA, whereas we did not observe a reduction of SUV39H1 activity across the tested dsRNA concentrations (Fig. 2c). Thus, we conclude that SUV39H2 KMT activity can be modulated by MajSat dsRNA. To address whether RNA modulation of SUV39H2 activity also occurs in vivo, we microinjected *in vitro* transcribed pericentromeric dsRNA into the paternal pronucleus of mid-stage zygotes<sup>20</sup> and interrogated global levels of H3K9me3 in late zygotes (Fig. 2d). Remarkably, H3K9me3 was undetectable in the paternal pronuclei of zygotes in which we injected pericentromeric dsRNA, but not single-stranded RNA (ssRNA) (Fig. 2e,f; Extended Data Fig. 2a,b). To further assess whether endogenous MajSat transcripts can regulate H3K9me3, we targeted VP64 to MajSat using TALE<sup>21</sup> in zygotes to activate the endogenous locus. Consistent with the above-described results, this led to a reduction of H3K9me3 throughout the paternal pronucleus (Fig. 2g,h). Thus, pericentromeric RNA has a regulatory function and can inhibit endogenous SUV39H2 activity, which in turn attenuates H3K9me3 levels in the early mouse embryo.

**H3K9me3 is non-repressive during early preimplantation development.** Next, we addressed the biological significance of de novo H3K9me3 catalysed by SUV39H2. For this, we first analysed H3K9me3 ChIP-seq data from zygotes from C57BL/6 × DBA crosses<sup>12</sup>. We sorted genes on the basis of their enrichment of H3K9me3 on either the paternal (DBA) or maternal (C57BL/6) chromatin. This analysis revealed a few genes with strong H3K9me3 enrichment on the paternal allele (Fig. 3a,b), which indicates that there is de novo H3K9me3 accumulation on these regions. This result was in agreement with our immunostaining results and with a previous ChIP-seq analysis<sup>12</sup>. As expected, H3K9me3 was also present across the maternal genome (Fig. 3a,b). Likewise, H3K9me3 was enriched at some repeat families on the paternal chromatin, particularly across Long Terminal Repeat (LTR)-containing retrotransposons, in agreement with a previous analysis<sup>12</sup> (Extended Data Fig. 3a; Supplementary Table 1). Short Interspersed Nuclear Elements (SINEs) were generally found in regions enriched with paternal H3K9me3 (Extended Data Fig. 3a). Other transposable element (TE) types such as LTRs from the Endogenous Retrovirus K (ERV-K; intracisternal A particles (IAPs)) and Retrotransposon LTR (RLTR) families were clearly decorated with H3K9me3 peaks (Extended Data Fig. 3b). In contrast, most Long Interspersed Nuclear Element 1 (LINE-1) retrotransposons were found in regions depleted of paternal H3K9me3 (Extended Data Fig. 3a). We conclude that H3K9me3 is distributed on specific regions of the paternal genome.

Second, we asked whether de novo H3K9me3 regulates gene expression. For this, we first performed RNA sequencing (RNA-seq)

**Fig. 1 | De novo H3K9me3 occurs in the paternal pronucleus immediately after fertilization.** **a**, Violin plots showing absolute non-normalized *Suv39h1* single-cell expression data by qRT-PCR as described before<sup>11</sup>. The dashed line in each plot represents the median value, and values for individual embryos are indicated by dots. For **a** and **d** two independent experiments were performed. **b**, Immunostaining for SUV39H1 in the mouse late zygote, two-cell stage and eight-cell stage. A representative single confocal section is shown for both pronuclei (pronuclear stage 3–4) from 19 zygotes across four independent experiments and a single nucleus of the two-cell stage (16 embryos) and eight-cell stage (13 out of 17 embryos positive) from three independent experiments. The white dashed lines demarcate the nuclear membrane. **c**, Left: representative single z-confocal section projections for the indicated number of embryos stained with anti-H3K9me3 from two (early; 19 h post-hCG) or five (late; 27 h post-hCG) independent experiments. Paternal (arrows) and maternal pronuclei are indicated. Right: quantification of the total H3K9me3 signal in late zygotes. The plot depicts the mean ± s.e.m. ( $n = 45$  zygotes collected from 5 independent experiments). **d**, Violin plots showing absolute non-normalized *Suv39h2* single-cell expression data by qRT-PCR as described before<sup>11</sup>. The dashed line in each plot represents the median value. **e**, A representative single confocal section is shown for embryos immunostained with anti-SUV39H2 from one (eight-cell), three (two-cell) or four (late zygote) independent experiments. The total number of embryos analysed across the above-mentioned experiments are indicated. White dashed lines demarcate the nuclear membrane. **f**, Experimental design for knockdown of *Suv39h2* in zygotes. **g**, Representative maximum intensity projections of zygotes treated as in **f**. Arrows point to the paternal pronuclei. Five independent experiments were performed for *Suv39h2* knockdown and three for the control knockdown (RNAi *lacZ*). **h**, Quantification of H3K9me3 fluorescence intensity of images in **g**. H3K9me3 fluorescence intensities were normalized to the mean maternal H3K9me3 signal in non-injected zygotes per experiment. Data are presented as the mean ± s.e.m. ( $n =$  the total number of embryos analysed across experiments as indicated in **g**). Two-sided Mann-Whitney *U*-test was used for statistical analysis. Scale bars, 10 μm (**b,e,g**) or 20 μm (**c**). Statistical information is provided as source data.

in late two-cell-stage embryos after *Suv39h2* RNAi (Supplementary Table 2). Surprisingly, we found that only 141 genes were differentially expressed (DE) ( $P$ -adjusted  $< 0.05$ ), among which more

genes (60%;  $n = 83$ ) were downregulated after *Suv39h2* knockdown (Fig. 3c; Supplementary Table 3). In addition, only five TEs displayed significant changes in expression (Fig. 3d; Supplementary

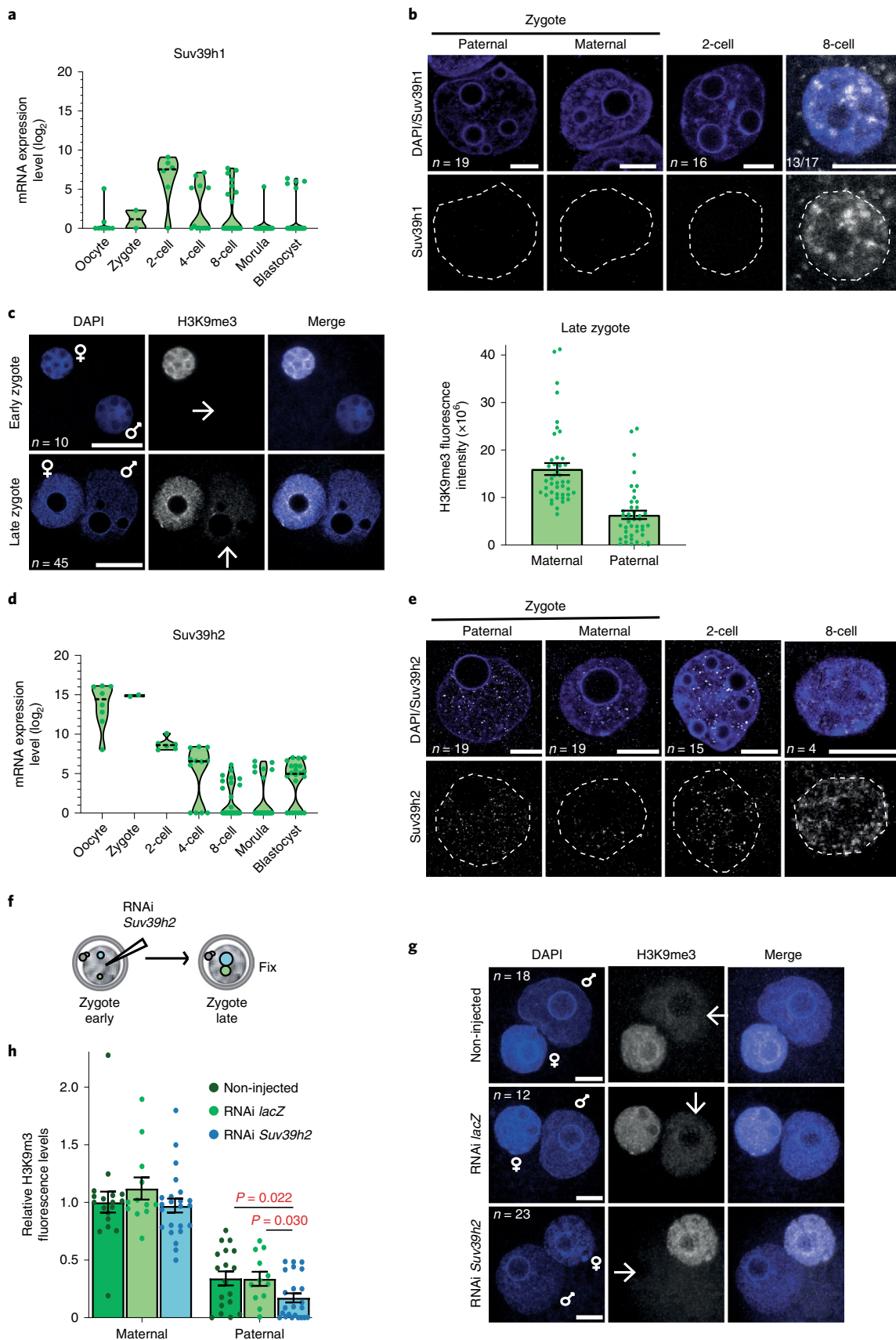


Table 3). We confirmed these results using quantitative PCR with reverse transcription (RT-qPCR) assays for selected genes and repeats (Extended Data Fig. 3c,d; Supplementary Table 4). Thus, de novo H3K9me3 catalysed by SUV39H2 is unlikely to regulate gene expression globally, including the expression of TEs. In line with our conclusions of a non-repressive role of de novo H3K9me3, we did not observe a major developmental defect after *Suv39h2* RNAi, since zygotes injected with dsRNA for *Suv39h2* formed blastocysts at a similar rate to control RNAi, and displayed no obvious morphological defects (Extended Data Fig. 3e).

Next, we addressed whether the few genes upregulated and downregulated after *Suv39h2* knockdown are enriched in H3K9me3. Remarkably, the majority of downregulated genes after *Suv39h2* RNAi were enriched in H3K9me3 at the transcription start site (TSS) in two-cell-stage embryos, acquiring signals from the mid-zygote to the late two-cell stage (Fig. 3e). In contrast, upregulated genes showed little or no enrichment of H3K9me3. Thus, depletion of *Suv39h2* results in the downregulation of some H3K9me3-enriched genes, which suggests that early deposition of H3K9me3 is compatible with gene expression. To address this hypothesis, we extracted the top 500 genes showing highest paternal and maternal H3K9me3 enrichment and investigated their expression throughout development using published RNA-seq datasets<sup>22</sup>. Transcripts of paternal H3K9me3-enriched genes were more abundant than the maternal H3K9me3-enriched counterpart (Fig. 3f). Many of these genes were robustly expressed, thus reinforcing the hypothesis that H3K9me3 is compatible with gene expression at these stages (Fig. 3g). However, differences in expression gradually resolved over cleavage stages (Fig. 3f), which implies that early marking of H3K9me3 may predispose for repression at later developmental times. To address this possibility, we first asked whether H3K9me3 enrichment correlates with chromatin accessibility. Surprisingly, an analysis of assay for transposase-accessible chromatin using sequencing (ATAC-seq) data of early embryos<sup>23</sup> revealed that genes paternally enriched with H3K9me3 displayed an average open chromatin configuration in early cleavage stages (Fig. 3h). Second, we assayed chromatin accessibility in embryos after *Suv39h2* depletion using nicking enzyme assisted sequencing (NicE-seq) (Extended Data Fig. 3f), which revealed that *Suv39h2* loss in zygotes results in an increased proportion of accessible promoters at the eight-cell stage (Fig. 3i). These data suggest that de novo H3K9me3 on the paternal chromatin primes genomic regions for chromatin compaction at later developmental stages. Importantly, our data indicate a non-repressive function of H3K9me3 at the beginning of development.

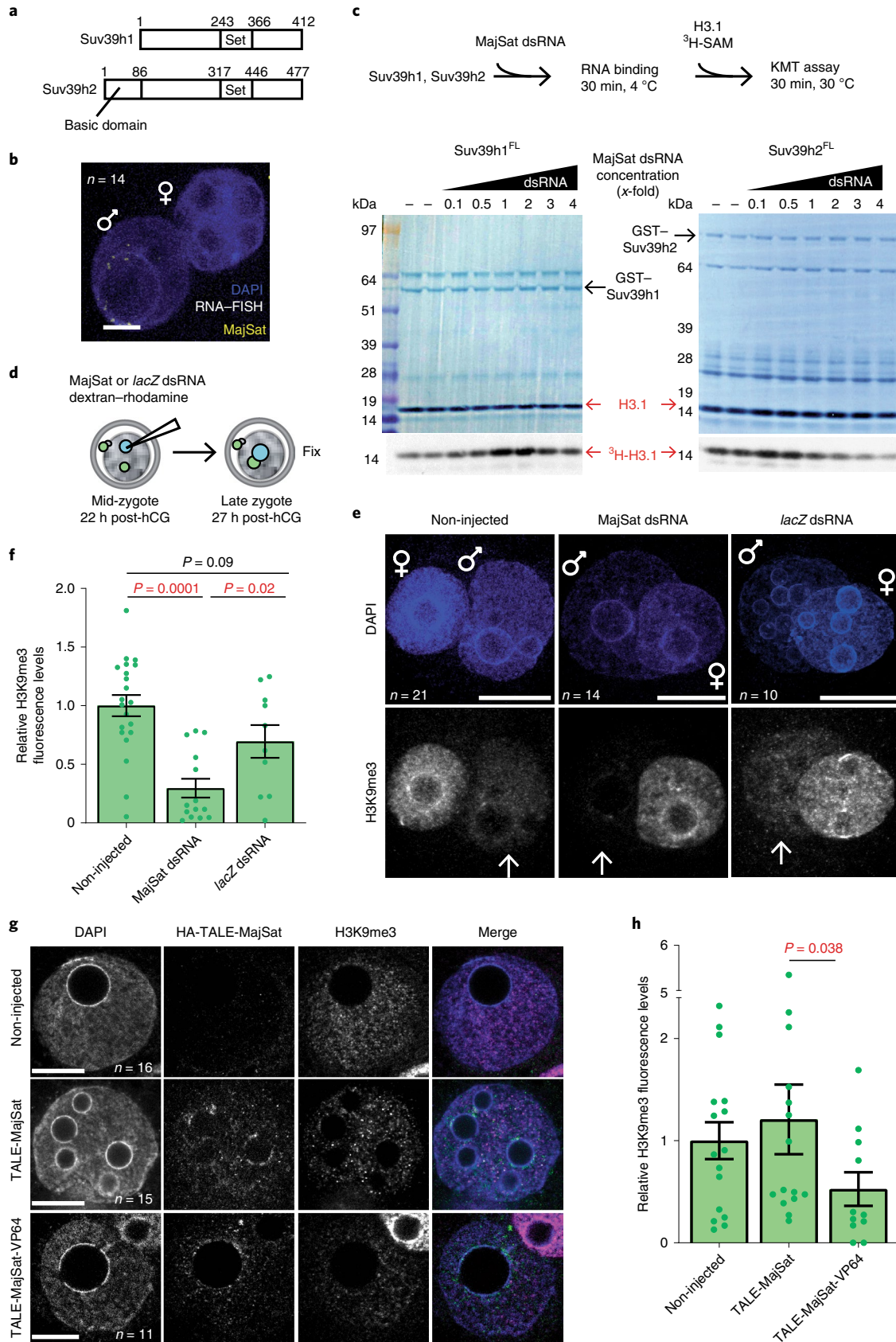
**Induction of constitutive heterochromatin compromises development.** Together, the above data indicate that the earliest developmental stages are characterized by a SUV39H2-driven H3K9me3 pathway, the activity of which is regulated by pericentromeric RNA and is largely non-repressive for gene expression. To address whether the absence of mature constitutive heterochromatin is due to the absence of SUV39H1 in early cleavage stages, we undertook a gain-of-function approach in zygotes (Fig. 4a). Microinjection of haemagglutinin-tagged wild-type *Suv39h1* (*HA-Suv39h1wt*) mRNA led to a robust expression of SUV39H1 in both pronuclei (Fig. 4b), which persisted until the four-cell stage, but not later (Fig. 4c; Extended Data Fig. 4a). Because ChIP approaches are not currently feasible in microinjected embryos, we addressed whether *Suv39h1wt* expression leads to global changes in chromatin using quantitative immunofluorescence. Expression of *Suv39h1wt* led to a robust increase in global H3K9me3 levels at the two-cell stage compared with controls (by  $2.7 \pm 0.15$ -fold) (Fig. 4d; Extended Data Fig. 4b; Supplementary Videos 1 and 2), which appeared distributed throughout the nucleus, with an obvious enrichment in regions rich in 4,6-diamidino-2-phenylindole (DAPI) staining. These DAPI-rich regions corresponded to regions of MajSat, as determined by labelling of these repeats using a dCas9-mClover fusion protein (Fig. 4e), which suggests that changes in nuclear organization of pericentromeric chromatin had occurred. Indeed, an analysis of Cenp-A and MajSat localization revealed a striking rearrangement of chromocentres at the two-cell stage, which appeared in stronger, fewer and more clustered foci in embryos expressing *Suv39h1wt* compared with controls (Fig. 4f,g). Thus, *Suv39h1wt* gain-of-function results in precocious chromocentre formation. The increase in global H3K9me3 in two-cell-stage embryos was specific to *Suv39h1*, since expression of equimolar concentrations of mRNA for other H3K9-specific methyltransferases (*Setdb1*, *Setdb2* or *Ehmt2* (also known as *G9a*)) did not lead to changes in global H3K9me3 levels to the extent of *Suv39h1wt* (Extended Data Fig. 4c,d). SUV39H1 activity also resulted in the accumulation of H4K20me3 in the pericentromeric chromatin<sup>24</sup> in a large proportion of embryos (Fig. 4g). In contrast, H4K20me3 was not detectable in the majority of control two-cell-stage embryos (Fig. 4g), as previously reported<sup>7,25</sup>. *Suv39h1wt* expression led to a robust accumulation of H3K64me3 throughout the nuclei of two-cell-stage embryos, which is contrary to the controls in which H3K64me3 is absent<sup>6</sup> (Fig. 4h; Extended Data Fig. 4e). We did not observe an increase in global levels of H3K9me3, H4K20me3 or H3K64me3 after expression of the catalytic dead enzyme (*Suv39h1mut*; Fig. 4d,g,h; Extended Data Fig. 4b,e; Supplementary Video 3). We conclude that expression of *Suv39h1wt* in zygotes leads to the premature establishment of

**Fig. 2 | Pericentromeric RNA modulation of the KMT activity of SUV39H2 attenuates H3K9me3 levels in the early preimplantation mouse embryo.**

**a**, Diagram depicting the alignment of *M. musculus* SUV39H1 (NP\_035644.1) and SUV39H2 (NP\_073561.2) proteins. The sequences have a 58% identity and 71% similarity, excluding the N-terminal basic domain. **b**, A representative full z-series confocal projection of RNA fluorescent in situ hybridization (RNA-FISH) for MajSat in 14 zygotes across 3 independent experiments. **c**, Top: schematic of in vitro KMT assays using full-length (FL) SUV39H1 or SUV39H2 after incubation with dsRNA from MajSat. Bottom: Coomassie (upper) and autoradiography (lower) images after the KMT assays. For SUV39H2, downregulation of activity is observed in four out of nine experiments (shown is a representative experiment of these four), whereas no downregulation is observed for SUV39H1 across seven experiments. **d**, Schematic of the experimental design. Zygotes were collected 22 h post-hCG injection and the paternal pronucleus was injected with MajSat or *lacZ* dsRNA and dextran-rhodamine as injection control. Zygotes were cultured for 5 h before fixation and immunostained with an anti-H3K9me3 antibody. **e**, Representative full z-series confocal projections of embryos manipulated as described in **d** from the indicated number of embryos across four independent experiments (three for RNAi *lacZ*). Arrows point to the paternal pronuclei. **f**, Quantification of the mean fluorescence intensity for H3K9me3 from images in **e**. Confocal stacks were reconstructed in 3D using Imaris, and the pronuclei were segmented using the DAPI channel. The average levels of H3K9me3 staining in the paternal pronucleus were quantified after background subtraction and normalized to the non-injected group. Shown is the mean  $\pm$  s.e.m. ( $n$ =the numbers indicated in **e**). Two-sided Mann-Whitney U-test was used for statistical analysis. **g**, Zygotes microinjected with HA-TALE-VP64 mRNA targeting MajSat or control HA-TALE-MajSat without VP64 were fixed at 27 h post-hCG (9 h later) and immunostained for anti-HA and anti-H3K9me3. Shown are representative single sections of confocal stacks for the indicated number of embryos from three independent experiments. **h**, Quantification of H3K9me3 levels in the paternal pronucleus across embryos from images in **g**. Data represent the mean  $\pm$  s.e.m. ( $n$ =the numbers indicated in **g**). Statistical analysis was performed using the two-sided Mann-Whitney U-test. Scale bars, 10  $\mu$ m (**b,e,g**). Statistical information and unprocessed blots are provided as source data.

constitutive heterochromatin and chromocentre formation, which suggests that the absence of SUV39H1 is the limiting factor controlling constitutive heterochromatin establishment after fertilization.

To address whether the delayed acquisition of constitutive heterochromatin is relevant for development, we tested the effect of *Suv39h1wt* expression on developmental progression (Fig. 5a).



Importantly, *Suv39h1wt* expression led to strong developmental arrest, with only 27% of embryos reaching the blastocyst stage, even after extended culture (Fig. 5b). In contrast, control non-injected embryos and embryos expressing green fluorescent protein (GFP) alone formed blastocysts at significantly higher rates of 93% and 75%, respectively (Fig. 5b). Embryos expressing *Suv39h1mut* developed at similar rates to the control injections, which demonstrates that the phenotype depends on SUV39H1 methyltransferase activity (Fig. 5b). The specific developmental arrest elicited by *Suv39h1wt* in comparison to *Suv39h1mut* appeared at the morula stage, without an obvious morphological effect on compaction (Extended Data Fig. 4h). These embryos showed misregulation of genes involved in pluripotency (*Myc* and *Klf4*) and lineage allocation (*Pdgfra*, *Pou5f1* (also known as *Oct4*), *Tead4*, *Gata6*, *Fgfr2* and *Cdx2*) (Extended Data Fig. 5a; Supplementary Tables 5 and 6). Accordingly, quantitative immunostaining and three-dimensional (3D) reconstruction of the *Suv39h1wt*-injected embryos that reached the blastocyst stage revealed a failure to segregate cells into the two blastocyst lineages and to fully repress *Nanog* in the trophectoderm (Extended Data Fig. 5b-d). This effect was specific to *Suv39h1*. Indeed, expression of *Suv39h2* in zygotes using the same experimental design as for *Suv39h1* (Fig. 5c) resulted in a similar increase in global H3K9me3 levels at the two-cell stage compared with *Suv39h1* (Fig. 5d,e). However, *Suv39h2* expression did not affect developmental progression, and embryos formed blastocysts in the same proportion as controls (Fig. 5f). In addition, ectopic expression of a different heterochromatic methyltransferase, *Suv420h1*, had no effect on embryo development<sup>26</sup>. Our results indicate that the acquisition of a global chromatin configuration with typical constitutive heterochromatic features, namely H3K9me3, H4K20me3, H3K64me3 and chromocentres, is not compatible with early developmental progression.

To investigate a potential effect of SUV39H1-mediated H3K9me3 on gene expression, we performed RNA-seq in late two-cell-stage embryos, the time point at which zygotic genome activation occurs<sup>27</sup>. Unexpectedly, our transcriptional profiling revealed only minor changes in gene expression between *Suv39h1wt* and control *Suv39h1mut*-injected groups (39 upregulated and 19 downregulated genes) (Fig. 6a; Supplementary Table 7). Similarly, most repeat families were unaffected (Fig. 6b; Supplementary Table 8). We validated our RNA-seq results using high-throughput RT-qPCR in single embryos, and these data confirmed no significant changes in the expression of the assayed genes or repetitive elements (Extended Data Fig. 6a; Supplementary Table 4). These experiments rule out a global downregulation of transcription in embryos expressing SUV39H1. We conclude that expression of SUV39H1 and the resulting increase in H3K9me3 do not drastically affect gene expression or zygotic genome activation at the two-cell stage.

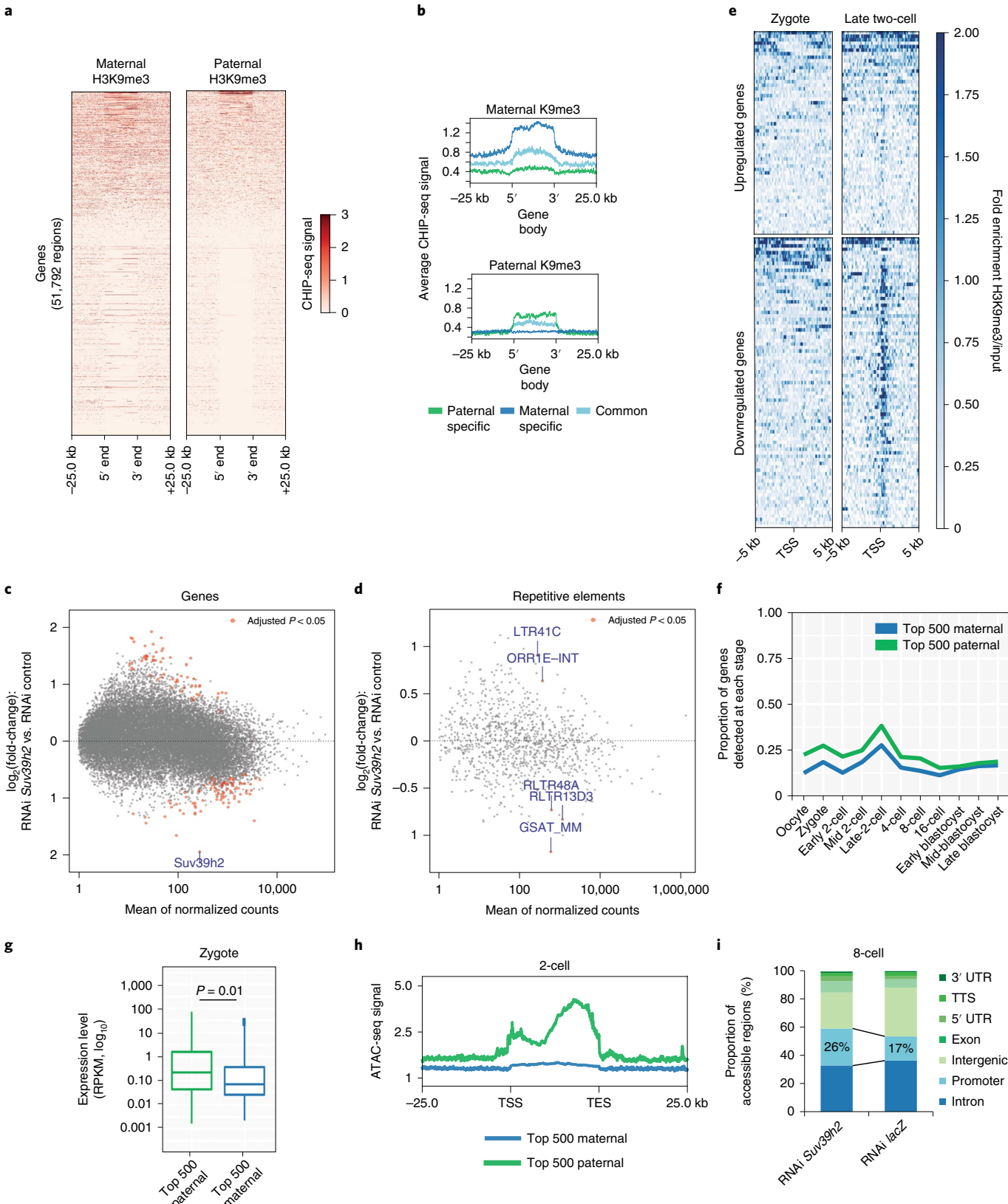
To address when gene expression changes arise and to assess potential phenotypic heterogeneity, we performed single-embryo RNA-seq at consecutive time points from the two-cell stage through to the morula stage, combined with pseudotime analysis (Supplementary Table 9). This revealed a defect in the gene expression programme at the four-cell stage in the majority of embryos expressing *Suv39h1wt* (Fig. 6c,d; Supplementary Table 10). We found 200 misregulated genes at this stage, the majority of which were upregulated (71%), thus supporting a non-repressive function for H3K9me3. Interestingly, we found that the majority of upregulated genes are normally specific to the two-cell stage (Fig. 6e). Thus, *Suv39h1* gain-of-function leads to a failure to downregulate a portion of the two-cell-stage gene expression programme. In addition we found that genes such as *Cdx2* (a regulator of the trophectoderm) and *Dppa1* (developmental pluripotency associated-1) were downregulated at the morula stage (Supplementary Table 10). Overall, our data suggest that the phenotype elicited after *Suv39h1wt* expression emerges heterogeneously at the four-cell stage partly due to defective downregulation of a significant fraction of the two-cell-stage gene expression programme and through the precocious formation of chromocentres, which culminates in the failure to achieve complete resolution of cell fate after blastocyst formation.

**SUV39H1 expression inhibits epigenetic reprogramming.** The above results suggest that enforcing SUV39H1-driven H3K9me3 and the consequent constitutive heterochromatic features after fertilization prevents epigenetic reprogramming in vivo. However, the above-described experimental setup does not distinguish between effects on development versus those on epigenetic reprogramming since they both occur in parallel during cleavage stages<sup>28</sup>. To directly address whether *Suv39h1wt* expression affects epigenetic reprogramming in vivo, we performed nuclear transfer (NT) in enucleated oocytes, using embryonic stem (ES) cell nuclei as donors (Fig. 7a). We microinjected *Suv39h1wt* mRNA after NT to enforce de novo H3K9me3 during reprogramming. Although depleting donor somatic nuclei of H3K9me3 before NT can improve cloning efficiency<sup>29</sup>, the role of de novo H3K9me3 at the onset of reprogramming, after NT, is unknown. We used two negative controls for potential micromanipulation effects: *Gfp* and *H2B-Cherry*. Expression of *Suv39h1wt* after NT resulted in a strong increase in H3K9me3 in two-cell-stage cloned embryos compared with the negative controls, which showed instead the typical dispersed H3K9me3 pattern after NT<sup>30,31</sup> (Fig. 7b, *H2B-Cherry*). Scoring the number of cloned embryos that developed past the two-cell stage, an indicator of successful reprogramming<sup>30,32</sup>, revealed a significantly lower rate of reprogramming with *Suv39h1wt* (*Gfp*:  $P=0.014$ ; *H2B-Cherry*:  $P=0.006$ ) (Fig. 7c). We also analysed the number of nucleolar-like bodies, which reflects changes in nuclear

**Fig. 3 | H3K9me3 is compatible with gene expression during early preimplantation development.** **a**, Heatmaps of zygotic H3K9me3 ChIP-seq signals over gene bodies, sorted by paternal pronucleus enrichment. Published H3K9me3 ChIP-seq data<sup>12</sup> were re-analysed for **a**, **b**, **e**, **f** and **g**. **b**, Metagene plots showing the distribution of maternal or paternal H3K9me3 over gene bodies. Genes were classified according to whether they overlapped a H3K9me3 peak exclusively in the maternal allele, exclusively in the paternal allele or in both alleles. **c,d**, RNA-seq performed on six pools for RNAi *Suv39h2*-injected and five pools for RNAi *lacZ*-injected embryos at the late two-cell stage (46 h post-hCG), collected from three independent experiments. Each pool consisted of five embryos. Differential expression analysis was performed using DESeq2. The MA plots depicts the  $\log_2$ (fold-change) in expression levels for genes (**c**) and repetitive elements (**d**) on the y axis against the mean expression on the x axis, with those with a significant change ( $P$ -adjusted  $< 0.05$ ) shown in red (listed in Supplementary Table 3). **e**, H3K9me3 ChIP-seq signals at the TSS ( $\pm 5$  kbp) of DE genes after *Suv39h2* knockdown versus knockdown control, in mid-zygote and late two-cell stage. Downregulated genes acquire clear H3K9me3 enrichment at the TSS by the two-cell stage. **f**, The proportion of top 500 maternal or paternal H3K9me3-marked genes expressed at each stage. The gene expression data for **f** and **g** were derived from ref. <sup>22</sup>. **g**, Expression levels of the top 500 maternal or paternal H3K9me3-marked genes in the zygote. The box plot depicts the median and interquartile range; whiskers span the range of the data, while extending no further than 1.5x the interquartile range. Two-sided Student's t-test was used to assess statistical significance. **h**, Average ATAC-seq signals in the two-cell stage over gene bodies of the top 500 zygotic H3K9me3-enriched genes in the maternal and paternal genomes. Data were derived from a published dataset<sup>23</sup>. TES, transcription end site. **i**, The proportion of genomic features enriched by NicE-seq in *Suv39h2* knockdown eight-cell stage embryos compared with controls. The total number of peaks identified was similar between the two conditions (12,449 versus 11,922). TTS, transcription termination site. Data shown represent results pooled from ten eight-cell-stage embryos across three independent experiments.

organization indicative of successful reprogramming<sup>33</sup>. *Suv39h1wt* led to a significant reduction in the number of nucleolar-like bodies ( $4.4 \pm 0.4$  versus  $6.7 \pm 0.4$ ,  $P = 1.1 \times 10^{-5}$ ) (Extended Data Fig. 6b). The decrease in the developmental capacity of cloned embryos

at the two-cell stage indicates a defect in reprogramming, which was progressively exacerbated since none of the embryos expressing *Suv39h1* after NT formed blastocysts (Fig. 7d; Extended Data Fig. 6c). The effect on NT efficiency was dependent on the



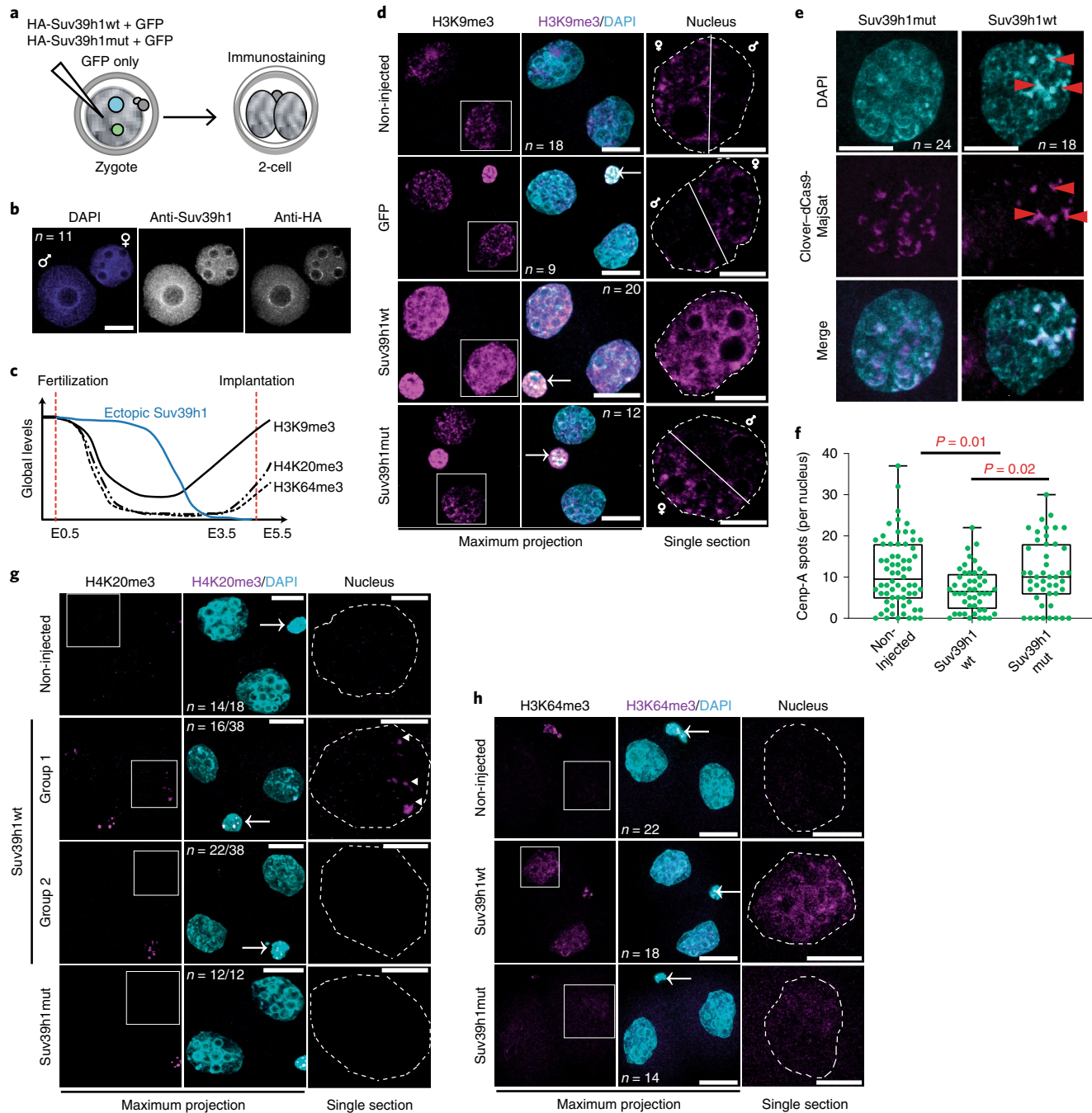


**Fig. 4 | SUV39H1 induces constitutive heterochromatin.** **a**, Diagram showing the experimental design. **b**, A representative full z-series projection of 11 zygotes injected with HA-Suv39h1 mRNA, fixed and immunostained with anti-SUV39H1 and anti-HA 8 h later from 3 independent experiments. **c**, Summary of the dynamics of global levels of heterochromatic histone modifications in the preimplantation mouse embryo and the transient ectopic SUV39H1 expression. **d**, Representative full z-series confocal projections for embryos manipulated as indicated in **a**. The right-hand panel depicts a representative single confocal section of an individual nucleus indicated by the boxed region on the H3K9me3 panel. The white solid line highlights the segregation of the maternal and paternal genomes in the controls but not Suv39h1wt-injected embryos (see Supplementary Videos 1–3 for 3D reconstructions). White dashed lines indicate the nuclear membrane (n = total number of embryos analysed across six independent experiments for Suv39h1wt and two for Suv39h1mut). Where visible, the polar body is indicated by an arrow in the merge panel. **e**, Zygotes microinjected with dCas9-mClover plus single guide RNAs targeting MajSats and HA-Suv39h1wt or HA-Suv39h1mut mRNA (18 h post-hCG) were fixed at the two-cell stage (42 h post-hCG) and immunostained with an anti-GFP antibody. A representative full z-series projection of the indicated number of embryos from five independent experiments is shown. Red arrowheads indicate DAPI-intense, MajSat-positive clusters. **f**, Mean number ( $\pm$ s.e.m.) of Cenp-A foci per nuclei was calculated by blind counting the number of embryos in **e**. Statistical analysis was performed using two-sided Mann-Whitney U-test. **g**, As for **d**, but for H4K20me3 (n = total number of embryos analysed across three independent experiments). The Suv39h1wt-injected group showed two patterns: either a strong increase around the nucleolar-like bodies (arrowheads) (group 1) or no H4K20me3 accumulation (group 2). The proportion of nuclei showing each pattern is indicated, determined through blind analysis. **h**, As for **d** but for H3K64me3 (n = total number of embryos analysed across five independent experiments for Suv39h1wt and four for Suv39h1mut). Scale bars, 10  $\mu$ m (**b,e** and nuclear zoom images for **d,g,h**) or 20  $\mu$ m (**d,g,h**). Statistical information is provided as source data.

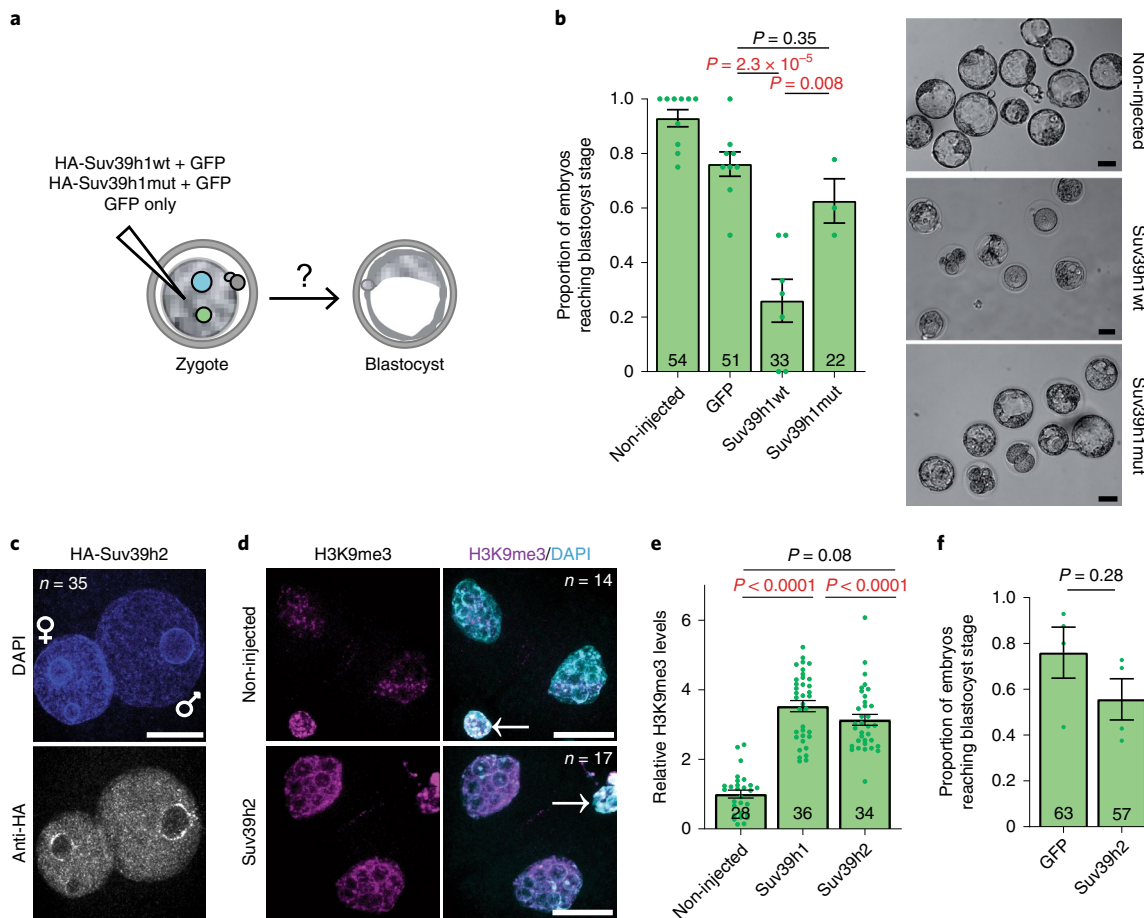


**Fig. 5 | SUV39H1 compromises development.** **a**, Diagram showing the experimental design. **b**, Left: the proportion of embryos that reached the blastocyst stage 72 h after microinjection. Data shown represent the mean  $\pm$  s.e.m. ( $n$  = the total number of embryos analysed as indicated on the graph across six independent experiments for *Suv39h1wt* and three independent experiments for *Suv39h1mut*). Statistical analysis was performed using N-1 Chi-squared test for comparing independent proportions. Right: representative bright-field images of embryos injected at the zygote stage with *Suv39h1wt* or *Suv39h1mut* mRNA and cultured to the blastocyst stage (72 h after microinjection). **c**, A representative full z-series confocal projection of 35 zygotes injected with HA-*Suv39h2* mRNA, fixed and immunostained with anti-HA 8 h later from 3 independent experiments. **d**, Zygotes were microinjected with HA-*Suv39h2* mRNA and fixed at the two-cell stage, 24 h after microinjection and immunostained with an anti-H3K9me3 antibody. A representative full z-series confocal projection is shown from three independent experiments ( $n$  refers to the total number of embryos analysed). Where visible, the polar body is indicated by an arrow in the merge panel. **e**, Mean levels of H3K9me3 in the two-cell stage embryo after *Suv39h1wt* or *Suv39h2* mRNA injection for the embryos represented in **d**. Error bars represent the s.e.m. ( $n$  = the total number of embryos analysed as indicated on the graph across three independent experiments). Statistical analysis was performed using unpaired Student's *t*-test. **f**, The proportion of embryos that reached the blastocyst stage 72 h after microinjection. Data shown represent the mean  $\pm$  s.e.m. ( $n$  = the total number of embryos analysed as indicated on the graph across four independent experiments). Statistical analysis was performed using N-1 Chi-squared test. Scale bars, 10  $\mu$ m (**c**), 20  $\mu$ m (**d**) or 50  $\mu$ m (**b**). Statistical information is provided as source data.

methyltransferase activity of SUV39H1 (Extended Data Fig. 6e). Thus, SUV39H1 blocks epigenetic reprogramming after NT. Together, the above results show that SUV39H1-mediated H3K9me3 in early embryogenesis is detrimental for developmental progression and epigenetic reprogramming.

## Discussion

Our results suggest that both a stepwise expression profile and regulation of the methyltransferase activity of SUV39H enzymes ensures low levels of H3K9me3 after fertilization (Fig. 7e). In addition, SUV39H1 and SUV39H2 may target different genomic regions, which, together with their distinct temporal expression patterns, may contribute to the regulation of heterochromatin establishment in the embryo. Assessing direct targets of SUV39H1 and SUV39H2 will shed light on the refined mechanism of action of the two SUV39H enzymes. We propose that an ‘early’ immature

heterochromatin, which is characterized by low levels of constitutive heterochromatic histone modifications, lack of chromocentres and a globally relaxed chromatin organization, is enabled through RNA-regulated SUV39H2. This immature heterochromatin is a hallmark of early mammalian development and is compatible with transcriptional activity. The restriction of ‘late’ mature heterochromatin, which is characterized by heterochromatic histone modifications, chromocentres, transcriptional repression and a more compact chromatin architecture, is controlled by the regulated expression of SUV39H1 and is essential for epigenetic reprogramming at fertilization.

We propose that de novo H3K9me3 after fertilization facilitates the subsequent establishment of ‘mature’ constitutive heterochromatin at around the time of implantation when other histone modifications of constitutive heterochromatin and DNA methylation start to accumulate<sup>2,34,35</sup>. This is in line with the self-regulatory

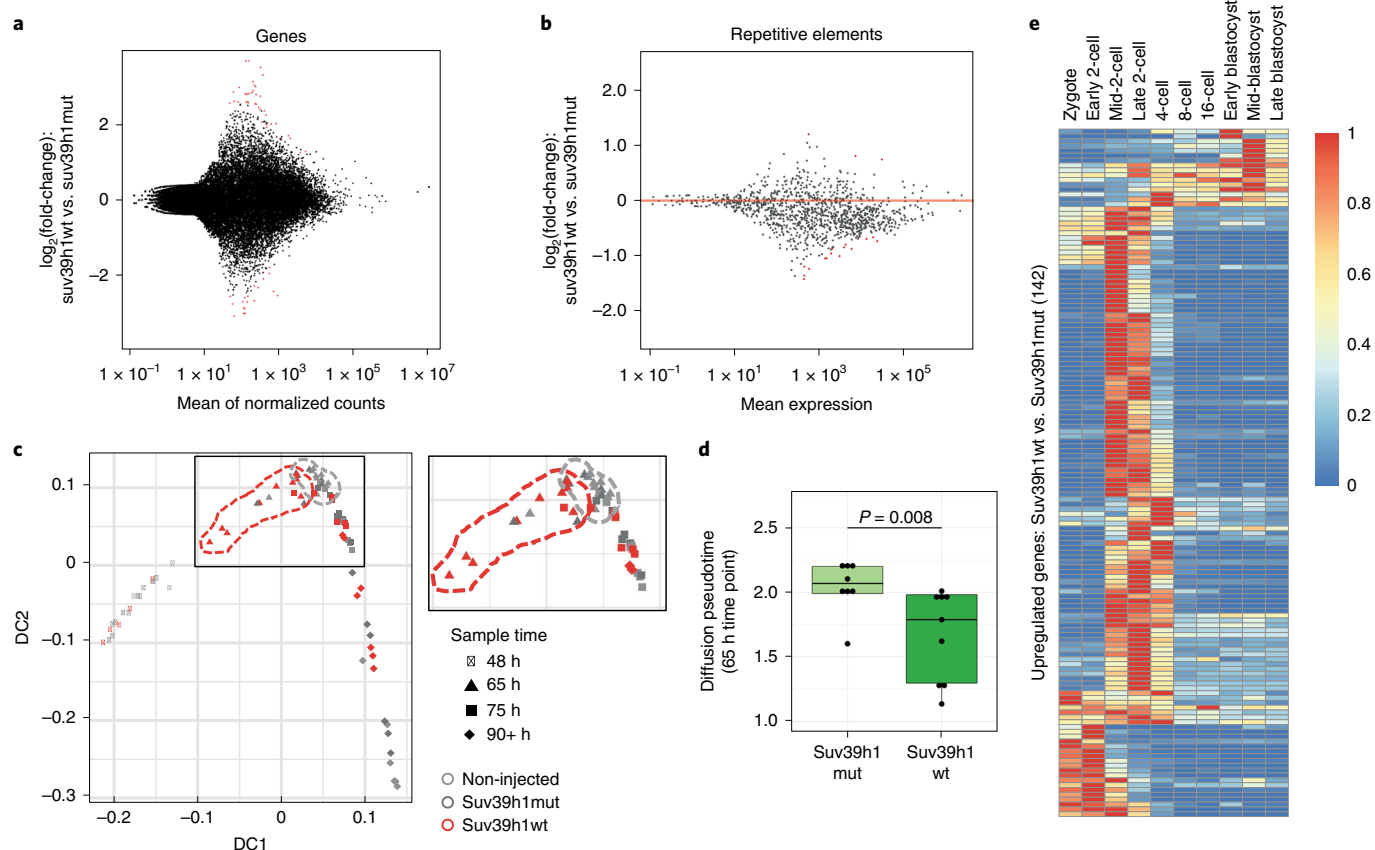


**Fig. 6 | SUV39H1 does not prevent zygotic genome activation.** **a,b**, RNA-seq was performed on embryos expressing *Suv39h1wt* and *Suv39h1mut* at the late two-cell stage (46 h post-hCG), in two pools of 20 embryos per condition; each pool was collected from three independent experiments. Differential expression analysis was performed using DESeq2. The MA plots depict  $\log_2(\text{fold-change})$  in gene (**a**) or repetitive element (**b**) expression levels against the mean expression, with those with a significant change ( $P$ -adjusted  $< 0.05$ ) shown in red (listed in Supplementary Tables 7 and 8). **c**, Diffusion map of the single-embryo RNA-seq RPKM counts. The areas enclosed by dashed lines indicate the relative positions of the *Suv39h1wt* embryos at 65 h (four-cell stage) in red and the combined controls at 65 h in grey. Embryos at all time points were collected from four independent experiments, including the three sample groups. **d**, Diffusion pseudotime distribution values of embryos expressing *Suv39h1wt* ( $n=9$ ) and *Suv39h1mut* ( $n=8$ ) at the 65 h time point ( $n$ =the indicated number of embryos from four independent experiments). The box plots represent the mean with interquartile ranges. Statistical analysis was performed using two-sided Mann-Whitney *U*-test. **e**, A heatmap depicting the endogenous expression patterns of the upregulated genes between embryos expressing *Suv39h1wt* versus *Suv39h1mut* at the 65 h time point (four-cell stage). Scaled RPKM counts are shown. RNA-seq datasets are from ref. <sup>22</sup>.

loop that directs and reinforces SUV39H1-dependent H3K9me3 methylation<sup>36</sup>. Once heterochromatin is established, H3K9me3 plays an important role in lineage establishment and maintenance<sup>37</sup>. The potential impact of SUV39H1 and SUV39H2 function and the resulting H3K9me3 on regulating DNA methylation dynamics during preimplantation development will be important to address in the future.

H3K9 modifiers can both inhibit and enhance induced pluripotent stem cell derivation<sup>38</sup>. During induced pluripotent stem cell generation, SUV39H1, but not SUV39H2, limits reprogramming efficiency to pluripotency<sup>39,40</sup>. Our data show that enforcing H3K9me3 via SUV39H1 during both natural reprogramming at fertilization and reprogramming to totipotency through NT is also detrimental for reprogramming, while SUV39H2-enabled immature heterochromatin is permissive. Additionally, it would seem that both the H3K9me3 status in the donor nuclei<sup>29,41</sup> and the de novo acquisition of H3K9me3 during the first steps of reprogramming once the process has been initiated (this work) are key determinants in reprogramming efficiency. Indeed, ectopic expression of the H3K9 demethylase *Kdm4b* in cloned embryos results in improved NT efficiency<sup>42</sup>. Together, this anticipates a dynamic mechanism whereby a turnover of H3K9me3 levels occurs at different steps of the process.

Our work further indicates that SUV39H1/SUV39H2-mediated H3K9me3 does not regulate the transposon repertoire in early development, which is in contrast to ES cells<sup>8</sup>. This is in line with recent work indicating that loss of SETDB1, while depleting H3K9me3 from a number LTRs, for the most part does not affect their transcription at the morula stage<sup>12,43</sup>. In addition, loss of EHMT2 does not lead to significant changes in TE expression<sup>44</sup>. The reported lack of HP1 $\alpha$  expression during preimplantation development<sup>7</sup>, along with other downstream heterochromatic features such as histone deacetylase activity, may explain the observed non-repressive function of H3K9me3. Nucleosome occupancy<sup>12</sup> may also be a more relevant mediator of transcriptional silencing in the early embryo. Recent work also indicates a non-canonical and transcriptional-neutral accumulation of H3K4me3 in oocytes<sup>45,46</sup>, which implies that a non-instructive role for histone modifications in transcriptional regulation may be a widespread feature of early development.

Our work underscores an important role for the dynamic regulation of H3K9me3 levels in the early mouse embryo, identifying a non-repressive function for H3K9me3, and documents a previously unappreciated regulatory role for RNA in restricting heterochromatic H3K9me3 at fertilization.

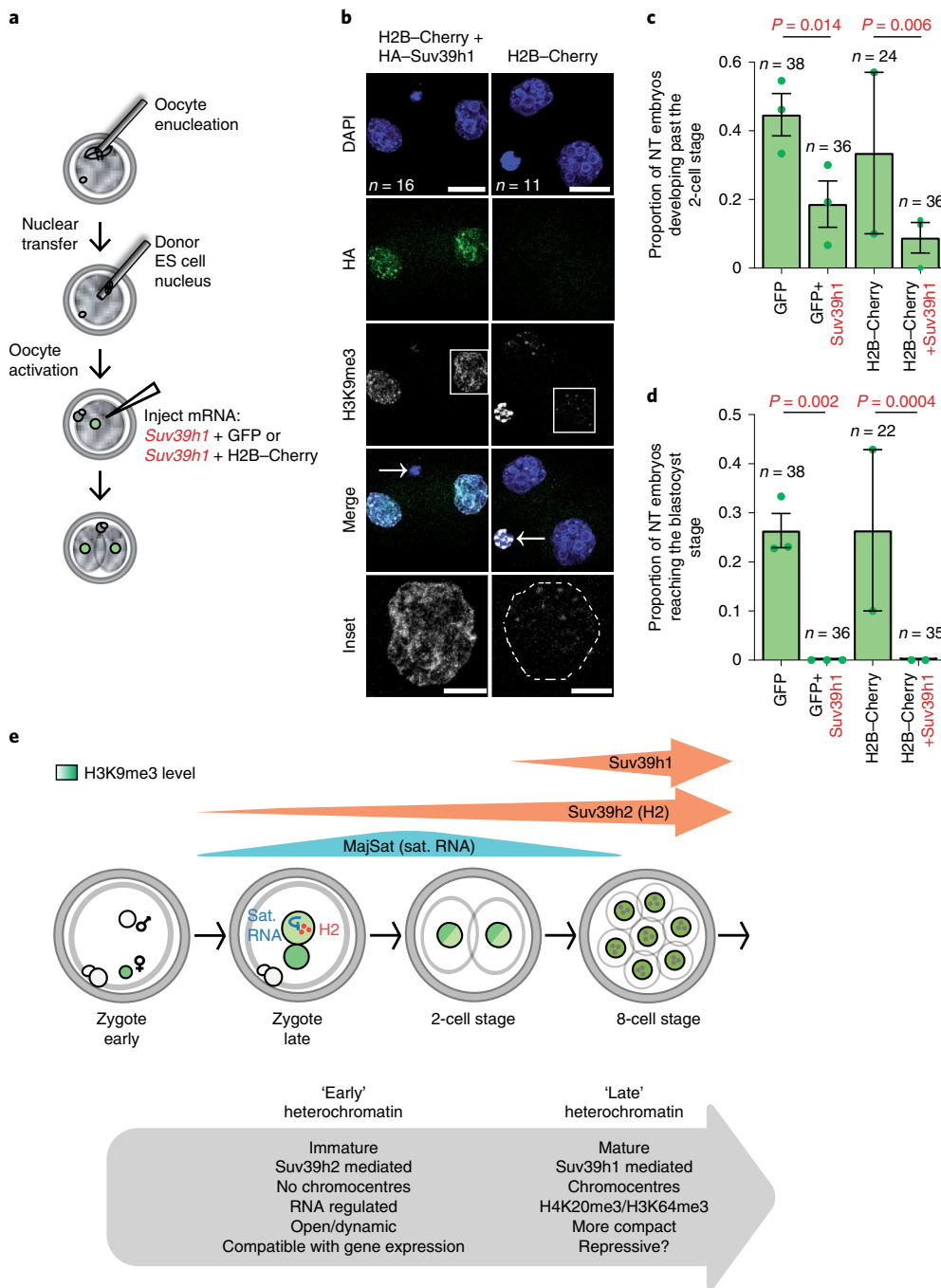


**Fig. 7 | SUV39H1 inhibits epigenetic reprogramming.** **a**, Experimental design for NT and microinjection. NT was performed using an ES cell nucleus as the donor. Four hours after activation, oocytes were microinjected with mRNA for *Suv39h1wt* and *Gfp* or *Gfp* alone or using an alternative control *Suv39h1wt* and *H2B-Cherry* or *H2B-Cherry* alone and cultured until the blastocyst stage. **b**, Representative full confocal z-series projections of embryos manipulated as described in **a** fixed at the two-cell stage and immunostained with anti-HA and anti-H3K9me3 antibodies ( $n$ =total number of embryos analysed from four independent experiments). The inset shows a higher magnification of the H3K9me3 staining in the boxed single nucleus. White dashed lines indicate the nuclear membrane in the control inset panel and the polar body is indicated by an arrow in the merge panel. Scale bar, 20  $\mu$ m (10  $\mu$ m for insets). **c**, The proportion of embryos developing beyond the two-cell stage. Data shown represent the mean  $\pm$  s.e.m. ( $n$ =the total number of embryos analysed as indicated on the graph across three independent experiments, except for *H2B-Cherry* alone, for which two independent experiments were performed). Statistical analysis was performed using N-1 Chi-square test for comparing independent proportions. **d**, The proportion of NT embryos developing to the blastocyst stage. Data shown represent the mean  $\pm$  s.e.m. ( $n$ =the total number of embryos analysed as indicated on the graph across three independent experiments, except for *H2B-Cherry* alone, for which two independent experiments were performed). Statistical analysis was performed using N-1 Chi-squared test. **e**, Schematic of a model summarizing our findings. Statistical information is provided as source data.

### Online content

Any methods, additional references, Nature Research reporting summaries, source data, extended data, supplementary information,

acknowledgements, peer review information; details of author contributions and competing interests; and statements of data and code availability are available at <https://doi.org/10.1038/s41556-020-0536-6>.

Received: 26 November 2017; Accepted: 24 May 2020;  
Published online: 29 June 2020

## References

- Arney, K. L., Bao, S., Bannister, A. J., Kouzarides, T. & Surani, M. A. Histone methylation defines epigenetic asymmetry in the mouse zygote. *Int. J. Dev. Biol.* **46**, 317–320 (2002).
- Burton, A. & Torres-Padilla, M. E. Chromatin dynamics in the regulation of cell fate allocation during early embryogenesis. *Nat. Rev. Mol. Cell Biol.* **15**, 723–734 (2014).
- Santos, F., Peters, A. H., Otte, A. P., Reik, W. & Dean, W. Dynamic chromatin modifications characterise the first cell cycle in mouse embryos. *Dev. Biol.* **280**, 225–236 (2005).
- Puschendorf, M. et al. PRC1 and Suv39h specify parental asymmetry at constitutive heterochromatin in early mouse embryos. *Nat. Genet.* **40**, 411–420 (2008).
- Santenard, A. & Torres-Padilla, M. E. Epigenetic reprogramming in mammalian reproduction: contribution from histone variants. *Epigenetics* **4**, 80–84 (2009).
- Daujat, S. et al. H3K64 trimethylation marks heterochromatin and is dynamically remodeled during developmental reprogramming. *Nat. Struct. Mol. Biol.* **16**, 777–781 (2009).
- Wongtawan, T., Taylor, J. E., Lawson, K. A., Wilmut, I. & Pennings, S. Histone H4K20me3 and HP1 $\alpha$  are late heterochromatin markers in development, but present in undifferentiated embryonic stem cells. *J. Cell Sci.* **124**, 1878–1890 (2011).
- Bulut-Karslioglu, A. et al. Suv39h-dependent H3K9me3 marks intact retrotransposons and silences LINE elements in mouse embryonic stem cells. *Mol. Cell* **55**, 277–290 (2014).
- Lachner, M., O'Carroll, D., Rea, S., Mechtler, K. & Jenuwein, T. Methylation of histone H3 lysine 9 creates a binding site for HP1 proteins. *Nature* **410**, 116–120 (2001).
- Peters, A. H. et al. Loss of the Suv39h histone methyltransferases impairs mammalian heterochromatin and genome stability. *Cell* **107**, 323–337 (2001).
- Burton, A. et al. Single-cell profiling of epigenetic modifiers identifies PRDM14 as an inducer of cell fate in the mammalian embryo. *Cell Rep.* **5**, 687–701 (2013).
- Wang, C. et al. Reprogramming of H3K9me3-dependent heterochromatin during mammalian embryo development. *Nat. Cell Biol.* **20**, 620–631 (2018).
- Burton, A. & Torres-Padilla, M. E. Epigenetic reprogramming and development: a unique heterochromatin organization in the preimplantation mouse embryo. *Brief. Funct. Genomics* **9**, 444–454 (2010).
- O'Carroll, D. et al. Isolation and characterization of Suv39h2, a second histone H3 methyltransferase gene that displays testis-specific expression. *Mol. Cell. Biol.* **20**, 9423–9433 (2000).
- Velazquez Camacho, O. et al. Major satellite repeat RNA stabilize heterochromatin retention of Suv39h enzymes by RNA-nucleosome association and RNA:DNA hybrid formation. *eLife* **6**, e25293 (2017).
- Johnson, W. L. et al. RNA-dependent stabilization of SUV39H1 at constitutive heterochromatin. *eLife* **6**, e25299 (2017).
- Shirai, A. et al. Impact of nucleic acid and methylated H3K9 binding activities of Suv39h1 on its heterochromatin assembly. *eLife* **6**, e25317 (2017).
- Maison, C. et al. Higher-order structure in pericentric heterochromatin involves a distinct pattern of histone modification and an RNA component. *Nat. Genet.* **30**, 329–334 (2002).
- Probst, A. V. et al. A strand-specific burst in transcription of pericentric satellites is required for chromocenter formation and early mouse development. *Dev. Cell* **19**, 625–638 (2010).
- Santenard, A. et al. Heterochromatin formation in the mouse embryo requires critical residues of the histone variant H3.3. *Nat. Cell Biol.* **12**, 853–862 (2010).
- Miyanari, Y., Ziegler-Birling, C. & Torres-Padilla, M. E. Live visualization of chromatin dynamics with fluorescent TALEs. *Nat. Struct. Mol. Biol.* **20**, 1321–1324 (2013).
- Deng, Q., Ramskold, D., Reinius, B. & Sandberg, R. Single-cell RNA-seq reveals dynamic, random monoallelic gene expression in mammalian cells. *Science* **343**, 193–196 (2014).
- Wu, J. et al. The landscape of accessible chromatin in mammalian preimplantation embryos. *Nature* **534**, 652–657 (2016).
- Probst, A. V., Santos, F., Reik, W., Almouzni, G. & Dean, W. Structural differences in centromeric heterochromatin are spatially reconciled on fertilisation in the mouse zygote. *Chromosoma* **116**, 403–415 (2007).
- Fadloun, A. et al. Chromatin signatures and retrotransposon profiling in mouse embryos reveal regulation of LINE-1 by RNA. *Nat. Struct. Mol. Biol.* **20**, 332–338 (2013).
- Eid, A., Rodriguez-Terres, D., Burton, A. & Torres-Padilla, M. E. SUV4-20 activity in the preimplantation mouse embryo controls timely replication. *Genes Dev.* **30**, 2513–2526 (2016).
- Schultz, R. M. The molecular foundations of the maternal to zygotic transition in the preimplantation embryo. *Hum. Reprod. Update* **8**, 323–331 (2002).
- Surani, M. A., Hayashi, K. & Hajkova, P. Genetic and epigenetic regulators of pluripotency. *Cell* **128**, 747–762 (2007).
- Matoba, S. et al. Embryonic development following somatic cell nuclear transfer impeded by persisting histone methylation. *Cell* **159**, 884–895 (2014).
- Ribeiro-Mason, K. et al. Nuclear dynamics of histone H3 trimethylated on lysine 9 and/or phosphorylated on serine 10 in mouse cloned embryos as new markers of reprogramming? *Cell. Reprogram.* **14**, 283–294 (2012).
- Liu, H., Kim, J. M. & Aoki, F. Regulation of histone H3 lysine 9 methylation in oocytes and early pre-implantation embryos. *Development* **131**, 2269–2280 (2004).
- Ogura, A., Inoue, K. & Wakayama, T. Recent advancements in cloning by somatic cell nuclear transfer. *Philos. Trans. R. Soc. Lond. B Biol. Sci.* **368**, 20110329 (2013).
- Martin, C. et al. Architectural reorganization of the nuclei upon transfer into oocytes accompanies genome reprogramming. *Mol. Reprod. Dev.* **73**, 1102–1111 (2006).
- Hemberger, M., Dean, W. & Reik, W. Epigenetic dynamics of stem cells and cell lineage commitment: digging Waddington's canal. *Nat. Rev. Mol. Cell Biol.* **10**, 526–537 (2009).
- Smith, Z. D. et al. A unique regulatory phase of DNA methylation in the early mammalian embryo. *Nature* **484**, 339–344 (2012).
- Rea, S. et al. Regulation of chromatin structure by site-specific histone H3 methyltransferases. *Nature* **406**, 593–599 (2000).
- Nicetto, D. et al. H3K9me3-heterochromatin loss at protein-coding genes enables developmental lineage specification. *Science* **363**, 294–297 (2019).
- Wei, J. et al. KDM4B-mediated reduction of H3K9me3 and H3K36me3 levels improves somatic cell reprogramming into pluripotency. *Sci. Rep.* **7**, 7514 (2017).
- Onder, T. T. et al. Chromatin-modifying enzymes as modulators of reprogramming. *Nature* **483**, 598–602 (2012).
- Soufi, A., Donahue, G. & Zaret, K. S. Facilitators and impediments of the pluripotency reprogramming factors' initial engagement with the genome. *Cell* **151**, 994–1004 (2012).
- Antony, J., Oback, F., Chamley, L. W., Oback, B. & Laible, G. Transient JMJD2B-mediated reduction of H3K9me3 levels improves reprogramming of embryonic stem cells into cloned embryos. *Mol. Cell. Biol.* **33**, 974–983 (2013).
- Liu, W. et al. Identification of key factors conquering developmental arrest of somatic cell cloned embryos by combining embryo biopsy and single-cell sequencing. *Cell. Discov.* **2**, 16010 (2016).
- Hatanaka, Y. et al. Histone chaperone CAF-1 mediates repressive histone modifications to protect preimplantation mouse embryos from endogenous retrotransposons. *Proc. Natl. Acad. Sci. USA* **112**, 14641–14646 (2015).
- Zylicz, J. J. et al. G9a regulates temporal preimplantation developmental program and lineage segregation in blastocyst. *eLife* **7**, e33361 (2018).
- Hanna, C. W. et al. MLL2 conveys transcription-independent H3K4 trimethylation in oocytes. *Nat. Struct. Mol. Biol.* **25**, 73–82 (2018).
- Zhang, B. et al. Allelic reprogramming of the histone modification H3K4me3 in early mammalian development. *Nature* **537**, 553–557 (2016).

**Publisher's note** Springer Nature remains neutral with regard to jurisdictional claims in published maps and institutional affiliations.

© The Author(s), under exclusive licence to Springer Nature Limited 2020

## Methods

**Reagents.** Unless otherwise stated all reagents were purchased from Sigma-Aldrich.

**Embryo collection, microinjection and culture.** All mouse experiments were approved by the Ethics Committee of the Université de Strasbourg (Cométh Institute of Genetics, Molecular and Cellular Biology) and performed under the compliance of French legislation or of the Government of Upper Bavaria. For immunostaining, CD-1 female mice (4–8 weeks old) were mated with CD-1 male mice (3–6 months old), and early and late zygotes, two-cell and eight-cell stages were collected at 10 h, 17 h, 38 h and 58 h post-coitum, respectively. For microinjection, embryos were collected from 5–7-week-old F<sub>1</sub> (C57BL/6J × CBA/H) superovulated females crossed with F<sub>1</sub> males (3–6 months old). Superovulation was induced by an intraperitoneal injection of pregnant mare serum gonadotropin (Intervet, 5 IU) and human chorionic gonadotropin (hCG; Intervet, 7.5 IU) 46–48 h later. Embryos were collected at the time points after hCG injection indicated in the figure legends. mRNAs were transcribed in vitro from the pRN3P plasmid using a mMESSAGE mMACHINE kit (Ambion). All complementary DNAs were subcloned to include identical 5' cap and untranslated region (UTR) (including Kozak) and 3' UTR to ensure equivalent expression levels. *Suv39h1* cDNA was a gift from A. J. Bannister (Gurdon Institute, Cambridge, UK). *Suv39h1mut* was prepared by site-directed mutagenesis of *Suv39h1* at histidine 324 to lysine and cysteine 326 to alanine<sup>36</sup>. Zygotes were microinjected with 1–2 pl of the indicated mRNAs (600 ng  $\mu$ l<sup>-1</sup> for *Suv39h1*, *Suv39h1mut* or *Suv39h2* or 250 ng  $\mu$ l<sup>-1</sup> for GFP) and randomly allocated to the experimental groups. Equimolar concentrations of *Setdb1* (1.5  $\mu$ g  $\mu$ l<sup>-1</sup>), *Setdb2* (900 ng  $\mu$ l<sup>-1</sup>) or *Ehmt2* (1.5  $\mu$ g  $\mu$ l<sup>-1</sup>) mRNA were microinjected. Embryos were cultured in K-modified simplex optimized medium microdrops under oil at 37 °C, 5% CO<sub>2</sub>. The dCas9-mClover plasmid was provided by T. Nakatani, and we microinjected 50–100 ng  $\mu$ l<sup>-1</sup> of mRNA and 20 ng  $\mu$ l<sup>-1</sup> of MajSat single guide RNA<sup>47</sup>. The TALE-MajSat control and TALE-VP64 mRNAs were microinjected at 600 ng  $\mu$ l<sup>-1</sup>.

**In vitro dsRNA preparation.** Double-stranded MajSat RNA was prepared as previously described<sup>20</sup> by in vitro transcription from pGEM plasmid (Clontech, A1360) containing a 234-bp MajSat repeat unit using a MAXIscript SP6/T7 kit (Ambion). This was followed by hybridization of the two complementary ssRNAs and treatment with RNaseA and T1 to remove non-hybridized ssRNA. A total of 1–2 pl of 700 ng  $\mu$ l<sup>-1</sup> MajSat dsRNA and 0.02% dextran–rhodamine was injected into the paternal pronucleus of zygotes. Single-stranded MajSat injection was performed with 1.4  $\mu$ g  $\mu$ l<sup>-1</sup> of the non-hybridized in-vitro-transcribed ssRNAs. dsRNA targeting *Suv39h2* was prepared by subcloning the N-terminal region of *Mus musculus Suv39h2* cDNA comprising base pairs 1–380 into the vector pGEM followed by in vitro transcription using the SP6 and T7 polymerases and then hybridization as described above. As a control, 500  $\mu$ g  $\mu$ l<sup>-1</sup> of a 460-bp region targeting the *lacZ* region comprising base pairs 1,568–1,957 was used. Purified dsRNA (500  $\mu$ g  $\mu$ l<sup>-1</sup>) was microinjected into zygotes with 0.02% dextran–rhodamine at the indicated times post-hCG. For in vitro histone methyltransferase assays, ssRNA was generated by in vitro transcription using the T7 promoter in the EcoRI-linearized pSAT plasmids<sup>48</sup> containing either a single repeat of MajSat cloned in the sense (pSAT-S) or antisense (pSAT-AS) orientation. To generate dsRNA, equimolar amounts of sense and antisense ssRNA were mixed in 1× SSC buffer (150 mM NaCl, 15 mM sodium citrate), incubated 2 min at 90 °C in a thermomixer. The temperature was allowed to drop to 60 °C and incubated for 5 min, then decreased to 20 °C and incubated for 30 min.

**Immunostaining and confocal microscopy.** Fixation of embryos was performed as previously described<sup>49</sup>. Briefly, the zona pellucida was removed with Acid Tyrode solution, followed by two washes in PBS and fixation in 4% paraformaldehyde, 0.04% Triton, 0.3% Tween-20, 0.2% sucrose at 37 °C. Embryos were then washed with PBS and permeabilized with 0.05% Triton X-100 for 20 min. After permeabilization, embryos were washed three times in PBST (0.1% Tween 20 in PBS), quenched in 2.6 mg ml<sup>-1</sup> freshly prepared ammonium chloride, washed three times in PBST and blocked for 3–4 h at 4 °C in blocking solution (3% BSA in PBST) and incubated with primary antibodies in blocking solution. Antibodies used were as follows: anti-SUV39H1 (Cell Signaling, 8729); anti-SUV39H2 (Abcam, 104343) (1:1,000); anti-HA (Roche, 11867423001); anti-H3K9me3 (Millipore, 07-442); anti-H3K9me3 (Active Motif, 39286) (1:100) (used only in relation to Fig. 1); anti-H4K20me3 (Millipore, 07-463); anti-H3K64me3 (a gift from S. Daujat IGBMC, France); anti-GFP (Abcam, ab13970) (1:1,000); anti-CENP-A/B (Europa Bioproducts, FZ90C-CS1058) (1:500); anti-CDX2 (BioGenex, AM392-5M) (1:500); anti-NANOG (CosmoBio, RCAB0002P-F) (1:500); and anti-OCT4 (BD Bioscience, 611203). Dilutions were 1:250 unless otherwise indicated. After overnight incubation at 4 °C, embryos were washed three times in PBST, blocked and incubated for 3 h at room temperature in blocking solution containing secondary antibodies labelled with Alexa or Cy3 fluorophores (Invitrogen) (catalogue numbers A32731, A32732, A32733, A10522, A-11029, A-21424, A32728 and A-21445, 1:500 dilution). After washing, embryos were mounted in Vectashield (Vector Laboratories) containing DAPI. Confocal microscopy was performed using a  $\times$ 63 oil objective in a TCS SP8 inverted confocal microscope (Leica). Z-sections

were taken every 0.5–1  $\mu$ m. Image analysis was performed using LAS-AF (Leica) and Imaris (Bitplane). For all experiments, acquisition parameters were set to obtain fluorescence intensity signals in the linear range of hybrid detectors. These detectors have negligible detector noise and linearly amplify incoming photons into photoelectrons, thereby allowing the counting of measured photons as long as the detector is not saturated. Hence, given identical acquisition settings, the recovered fluorescence signal accurately reflects the level of antigen present in the system

**Quantification of fluorescence intensity.** Confocal z-series stacks were reconstructed in 3D using Imaris (Bitplane), and the pronuclei (zygote) or nuclei (two-cell stage) were segmented based on the DAPI channel. We used 3D images because analysis of optical sections at 0.5- $\mu$ m apart robustly reflects the intensity distribution throughout the nucleus (for example, see refs. <sup>26,50</sup>) more accurately than measuring a single confocal section alone. The average fluorescence intensity for the channel of interest within the segmented region was calculated after background subtraction (based on the cytoplasmic signal). Because the use of a no-primary antibody control reliably resulted in a background signal intensity comparable to the cytoplasmic signal intensity, we chose to use the cytoplasmic signal as the threshold for background subtraction for nuclear antigens targeted in this study, as this should largely originate from secondary antibody nonspecific binding. The background threshold was calculated based on the mean cytoplasmic intensity plus two standard deviations of the cytoplasmic signal, thus corresponding to the empirical 95% rule and hence encompassing the majority of nonspecific intensity values. The fluorescence intensity for each embryo was normalized to the mean of the non-injected control group per experiment.

**NT and microinjection.** NT experiments were performed under authorization from the departmental veterinary regulatory service (license number 78-95) and from the local ethics committee (number 12/123, Comethea Jouy-en-Josas/AgroParisTech) at the INRA. Oocytes were prepared from superovulating 8-week-old F<sub>1</sub> (C57BL6 × CBA/H) mice by collecting from oviducts 14 h post-hCG (hours after injection of hCG) and washing in M2 medium containing 300 IU ml<sup>-1</sup> hyaluronidase to remove cumulus cells. Subsequently, they were incubated in M2 containing 5  $\mu$ g ml<sup>-1</sup> cytochalasin B and placed in a chamber on the stage of an inverted microscope (Olympus IX70) equipped with micromanipulators (Narishige, MO-188). The chromatin spindle (visualized under differential interference contrast) was aspirated as previously described<sup>51</sup>. The ES cells CK35, derived from 129Sv/Pas blastocysts (a gift from Pasteur Institute—Mouse Functional Genetics Unit), were used as donor cells. ES cells were synchronized in metaphase culture with 0.05  $\mu$ g ml<sup>-1</sup> of demecolcin for 2 h. Cells were gently aspirated in and out of the injection pipette (inner diameter of 7–8  $\mu$ m) followed by microinjection into the cytoplasm of the enucleated oocytes with a Piezo<sup>51,52</sup>. NT embryos were activated by incubating for 3 h in Ca<sup>2+</sup>-free medium containing 10 mM Sr<sup>2+</sup>. Embryos with visible nuclei, considered as activated, were transferred into fresh M16 medium and cultured at 37 °C in a humidified atmosphere containing 5% CO<sub>2</sub>. For microinjection, embryos were placed in M2 in a chamber on the stage of a Nikon inverted microscope equipped with Narishige micromanipulators and an Eppendorf microinjector. Embryos were microinjected in the cytoplasm with 1–2 pl of the indicated mRNAs (600 ng  $\mu$ l<sup>-1</sup> for *Suv39h1* or 250 ng  $\mu$ l<sup>-1</sup> for GFP or H2B-Cherry). Microinjections were performed at 4–5 h post-activation. Incubation was then carried out in M16 culture medium at 37 °C, 5% CO<sub>2</sub> for further development.

**RNA-seq and library preparation.** For the *Suv39h1*-injected pooled two-cell-stage analysis (Fig. 6a,b), control non-injected, *Suv39h1wt* or *Suv39h1mut*-injected embryos were collected at 46 h post-hCG, washed in PBS and flash-frozen in lysis buffer from a Single-Cell Lysis kit (Ambion, 4458235). Duplicates of 20 embryos pooled from three independent experiments were acquired for each experimental group. After thawing, embryos were subjected to DNase treatment with 1  $\mu$ l DNase, incubated for 5 min at room temperature, then 1  $\mu$ l of stop solution was added and incubated for 2 min, according to the manufacturer's instructions. Amplified cDNA was prepared from 2 ng of total RNA using an Ovation RNA-seq system V2 (NuGEN Technologies) following the manufacturer's instructions. Amplified cDNA was purified using AMPure XP beads (Beckman Coulter) and 500 ng was fragmented by sonication using a Covaris E210 instrument (with duty cycle of 10%, intensity of 5 and cycle/burst of 200 for 180 s). RNA-seq library preparation was performed using an Ovation Ultralow Library System kit (NuGEN Technologies) according to the manufacturer's instructions. DNA libraries were checked using a 2100 Bioanalyzer (Agilent) and quantified using a Kapa Sybr Fast Light Cycler 480 qPCR kit (Kapa Biosystems). The libraries were loaded in the flow cell at 14 pM concentration and sequenced using an Illumina HiSeq 2500. Image analysis and base calling were performed using RTA 1.18.61 and CASAVA 1.8.2.

For dsRNA *Suv39h2*-injected pooled two-cell-stage analysis (Fig. 3c,d), embryos were cultured until the two-cell stage (42 h post-hCG), and pools of ten two-cell-stage embryos were washed with PBS, placed in tubes with 1× lysis buffer (Takara, ST0948) and flash-frozen in liquid nitrogen. RNA-seq was carried out using the SMART-seq2 protocol, as previously described<sup>53</sup>, and subjected to paired-end sequencing on a Nextseq 500 (Illumina) platform. Notably, SMART-seq2, like all single-cell and low-input RNA-seq protocols available to

date, relies on poly(A)-based amplification; therefore, our RNA-seq was unable to identify nonpolyadenylated and cryptic transcripts. We analysed four to six biological replicates (pools of five) for each experimental group. The numbers of replicates and reads per sample are indicated in Supplementary Table 2.

For *Suv39h1* gain-of-function two-cell-stage to blastocyst single-embryo analysis (Fig. 6c,d), embryos were cultured until the indicated time points post-hCG, at which point a representative proportion of embryos was collected. Collections were obtained from four independent experiments. Individual embryos were washed with PBS, placed in tubes with 1× lysis buffer (Takara, ST0948) and flash-frozen in liquid nitrogen. RNA-seq was carried out using the SMART-seq2 protocol<sup>53</sup> and subjected to paired-end sequencing on a Nextseq 500 (Illumina) platform. The numbers of replicates and reads per sample are indicated in Supplementary Table 9.

**RNA-seq data analysis.** For the *Suv39h1*-injected pooled two-cell-stage analysis (Fig. 6a,b), reads were mapped onto the mm9 assembly of the *M. musculus* genome using Tophat (v.2.0.14)<sup>54</sup> and Bowtie (v.2-2.1.0)<sup>55</sup>. Quantification of gene expression was performed using HTSeq (v.0.6.1)<sup>56</sup> and gene annotations from Ensembl (release 67). Read counts were normalized across libraries as previously described<sup>57</sup> and data were analysed as previously described<sup>58</sup>, implemented in the DESeq2 Bioconductor library (DESeq2 v.1.14.1). Resulting *P* values were adjusted for multiple testing as previously described<sup>59</sup>. The following thresholds were used to select significantly DE genes: *P* value adjusted for multiple testing <0.05,  $|\log_{10} \text{fold-change}| > 1$ . Repeat analysis was performed as before<sup>58</sup> by aligning reads to repetitive elements in two passes. In the first pass, reads were aligned to the non-masked *M. musculus* reference genome (mm9) using Burrows–Wheeler aligner (v.0.6.2)<sup>60</sup>. Positions of the reads uniquely mapped to the *M. musculus* genome were cross-compared with the positions of the repeats extracted from UCSC (rmsk table in the UCSC database for *M. musculus* mm9), and reads overlapping a repeat sequence were annotated with the repeat family. In the second pass, reads not mapped or multi-mapped to the *M. musculus* genome in the previous pass were aligned to RepBase (v.18.07)<sup>61</sup> repeat sequences for rodent. Reads mapped to a unique repeat family were annotated with the family name. Finally, we summed the read counts per repeat family of the two annotation steps. Data were normalized based on library size and data were analysed as implemented in the DESeq2 Bioconductor library (DESeq2 v1.14.1)<sup>58</sup>. *P* values were adjusted for multiple testing using the Benjamini–Hochberg method.

For dsRNA *Suv39h2*-injected pooled two-cell-stage analysis (Fig. 3c,d), RNA-seq sequencing reads were trimmed using BBduk (<http://jgi.doe.gov/data-and-tools/bbtools>) with the following parameters: ktrim=r, k=23, mink=11, hdist=1, tbo, tpe. Trimmed reads were mapped to the GRCm38 *M. musculus* reference genome using STAR (v.2.5.2b) with the following parameters: --outFilterType BySJout --outFilterScoreMinOverRead 0.3 --outFilterMatchNminOverRead 0 --outFilterMismatchNmax 33 --seedSearchStartLmax 12 --alignSJoverhangMin 15. The HTSeq tool htseq-count (v.0.9.1) was used for read counting against the gene annotations downloaded from gencode (release M12, GRCm38.p5) with reverse strand setting. Differential expression analysis was performed using DESeq2 (v.1.18.1). The spike-in normalization factor was calculated from ERCC spike-in mix using the remove unwanted variation strategy from RUVseq (v.1.12.0). To calculate the spike-in normalization factor, genes with fewer than five reads in at least two samples were discarded. DESeq2 was run with the following design: spike-in normalization factor + conditions. Genes with normalized counts lower than two in at least four samples were discarded from the differential expression analysis. One of the replicates from the RNAi *lacZ* condition was discarded from the analysis due to the unexpected number of reads mapped to the ERCC spike-in and clustering outlier in the quality control analysis, indicating technical failure. Genes with an adjusted *P* value of ≤0.05 were considered significantly DE. The IfcShrink function from DESeq2 was used for visualization purposes. Differential repeat expression analysis was performed on reads remapped with STAR using the recommended parameters for TE transcripts as follows: --outFilterMultimapNmax 100 --winAnchorMultimapNmax 200. Ambiguously mapped reads were used for differential repeat expression analysis using TEtranscripts (v.2.0.3) with the following parameters: --stranded no --mode multi. Repeat annotations were downloaded from RepeatMasker (<http://www.repeatmasker.org/>), and repeats with the same identity were merged. Differential expression analysis was performed as described above using the count table generated from TEtranscripts.

For *Suv39h1* gain-of-function two-cell-stage to blastocyst single-embryo analysis (Fig. 6c,d), reads were cleaned of adapters using Trimmomatic (v.0.38)<sup>62</sup>, then Kallisto (v.0.44.0)<sup>63</sup> was used to align the reads to the mouse genome mm10 (GRCm38.p6). Quality control tests were carried out using the R packages Scater<sup>64</sup> and Single Cell Experiment by comparing the library size and ERCC counts, deleting the outlier embryos. Genes with an average number of counts of ≥10 were kept for subsequent analysis. Counts were normalized by reads per kilobase million (RPKM) using edgeR<sup>65</sup> and were used to plot a diffusion map with Destiny package<sup>66</sup>. The diffusion pseudotime was calculated by measuring the distance of the embryos to the tip corresponding to the two-cell stage. Pairwise differential gene expression analysis was done between the non-injected, *Suv39h1mut* and *Suv39h1wt* embryos, using the method implemented by DESeq2

(v.1.22.1)<sup>58</sup>. A normality test of Shapiro–Wilk was done, as the distributions were not normal when we performed a Wilcoxon test. DE genes between *Suv39h1mut* and *Suv39h1wt* embryos and expression in normal embryos was analysed using previously single-cell RNA-seq data<sup>22</sup>. A feature scaling normalization method was used for visualization of data between stages.

**Targeted qPCR high-throughput gene expression analysis.** Control non-injected, *Gfp*-only, *Suv39h1wt* or *Suv39h1mut*-injected embryos or dsRNA *Suv39h2*, dsRNA *lacZ* or non-injected embryos were washed in PBS and flash-frozen in liquid nitrogen in 5 µl of 2× reaction buffer (CellsDirect One-Step qRT-PCR kit, 11753100, ThermoFisher) at 46 or 78 h post-hCG for the two-cell-stage or morula-stage analyses, respectively. TaqMan Gene Expression assays (20× Applied Biosystems), previously tested using ES cell cDNA for amplification efficiency, were pooled to a final concentration of 0.2× for each of the 45 assays. To each of the single-cell samples in 2× reaction buffer, 2.5 µl of 0.2× assay pool, 0.5 µl RT/Taq enzyme (CellsDirect One-Step qRT-PCR kit, 11753100, ThermoFisher) and 2.3 µl of water were added. Cell lysis and sequence-specific reverse transcription were performed at 50 °C for 20 min. The reverse transcriptase was inactivated by heating to 95 °C for 2 min. Sequence-specific pre-amplification was performed by denaturing at 95 °C for 15 s, then annealing and amplification at 60 °C for 4 min for 18 cycles. The resulting cDNA was diluted fivefold before analysis with Universal PCR Master Mix and TaqMan Gene Expression assays (Applied Biosystems) in 48:48 Dynamic Arrays on a Biomark System (Fluidigm). For the two-cell-stage analysis, a DNase treatment was incorporated, as Taqman Gene Expression assays targeting repetitive elements were utilized immediately after cell lysis by incubation of the embryo in 4 µl of 2× reaction buffer with 2.5 µl DNase and 0.7 µl DNase buffer (CellsDirect One-Step qRT-PCR kit, 11753100, ThermoFisher) for 15 min at room temperature. The treatment was stopped by adding 5 mM EDTA and incubating for 10 min at 70 °C. Subsequently 5 µl of 2× reaction buffer, 0.4 µl of RT/Taq, 4.9 µl of assay pool and 2.5 mM of MgSO<sub>4</sub> were added and incubated for 20 min at 50 °C for reverse transcription. The following steps were identical to the above, except a tenfold dilution was carried out before qPCR analysis due to the high expression of some targets (for example, ribosomal DNAs and SINEs). Cycle threshold (Ct) values were calculated from the system's software (Biomark Real-time PCR analysis, Fluidigm). All raw Ct values were normalized to the assumed detection Ct level of 28 following recommendation from Fluidigm technical support<sup>11</sup>. Ct values greater than 28 and those with curve qualities lower than 0.65 were deemed unreliable measurements and had their Ct values substituted with 28. Whenever Ct values or quality scores were judged unreliable in one replicate, but not in the other, those of the successful replicate were kept. Additionally, all samples lacking expression of the reference genes *Actb* (which encodes actin-β) and *Gapdh* were removed from further analysis. The remaining Ct values were subtracted from 28 to achieve a scale in which zero corresponds to the lack of expression and an increase of 1 unit indicates a doubling of the expression level<sup>11</sup>. Violin plots of the resulting dataset were generated using the ggplot2 R package. Statistical analysis was performed using the Mann–Whitney *U*-test. For the *Suv39h1* (Fig. 1a) and *Suv39h2* (Fig. 1d) expression analysis during preimplantation development, detailed methods have been previously described<sup>11</sup>. Data are presented as absolute expression values.

**Methyltransferase assay.** The pGEX-6P1/*Suv39h1*/FL/BC and pGEX-6P1/*Suv39h2*FL/477/BC and plasmids were constructed by inserting synthetic genes (Integrated DNA technologies), which were optimized with bacterial codons, coding for murine SUV39H1 and SUV39H2 into the pGEX-6P1 plasmid using EcoRI and XhoI restriction sites. SUV39H1 and SUV39H2 proteins were expressed in BL21 gold bacterial cells. Cells were grown in 2xYT medium containing 100 µg ml<sup>-1</sup> ampicillin, induced with 0.4 mM isopropyl-β-D-1-thiogalactopyranoside when the OD<sub>600</sub> value was 0.8 and incubated overnight at 16 °C, after which cells were collected by centrifugation. Bacterial cells were lysed in a buffer containing 40 mM Tris-HCl pH 8.0, 9% glycerol, 2.5 mg ml<sup>-1</sup> and complete, EDTA-free protease inhibitor cocktail tablets. Lysate was digested with 25 U ml<sup>-1</sup> benzonase, mixed with a total of 0.5 M KCl, 0.1% NP40, 0.2% Triton X-100, sonicated (20 times 1 s on, 2 s off) and centrifuged at 4 °C, 12,000 × g for 30 min. Supernatants were affinity purified using glutathione sepharose 4B (purchased from GE Healthcare Life Sciences). To remove bacterial chaperones bound to the protein, after 2 h and 45 min of incubation of glutathione sepharose with lysate, 3 ml of supernatant was collected (per 0.5 litre of starting culture), incubated 5 min at 70 °C with rotation and then spun down at maximum speed for 1 min. Supernatant was mixed with the rest of the sepharose–lysate suspension and 1 mM of ATP and samples were incubated for 30 min. Glutathione sepharose was washed three times with 15 ml buffer containing 40 mM Tris-HCl pH 8.0, 0.5 M KCl, 9% glycerol, 0.1% Triton X-100, 0.1% NP40 and three times with 15 ml of the same buffer also containing 0.05 mM ZnCl<sub>2</sub>. Proteins were eluted with buffer containing 20 mM Tris-HCl pH 8.0, 0.5 M KCl, 9% glycerol, 1 mM dithiothreitol and 10 mM reduced glutathione pH 8.0. For the histone methyltransferase assay, purified proteins were pre-incubated with dsRNA for 30 min at 4 °C, mixed with 2.67 µM of recombinant histone H3.1, 6 µM hot 3H-SAM (1.5 µCi), and incubated for 30 min at 30 °C. SDS-PAGE was performed on the reaction mixtures and subsequently transferred to polyvinylidene fluoride membrane. The membranes

were stained with Amido Black and sprayed with enhancer, and autoradiography film was exposed for 1 h.

**Mouse embryonic fibroblast cells.** The *Suv39h1/2* double knockout mouse embryonic fibroblast cells have previously been characterized<sup>10</sup>.

**H3K9me3 ChIP-seq analysis.** Allele-specific H3K9me3 ChIP-seq signal tracks<sup>12</sup> were obtained as previously described<sup>37,68</sup> and normalized to input. H3K9me3 ChIP-seq has been extensively characterized<sup>12</sup>. Gene coordinates were obtained from Ensembl using Biomart, and the average ChIP-seq signal over the gene body was computed using BEDOPS' bedmap<sup>69</sup>. Heatmaps were generated using deepTools. For the metagene plots in Fig. 3b, peaks were called using the Epic implementation of the SICER algorithm<sup>70</sup> and genes were classified depending on whether they overlapped an H3K9me3 peak exclusively in the paternal allele, exclusively in the maternal allele or in both alleles. We used the Epic implementation of the SICER algorithm because it is more appropriate for calling peaks at a broader domain. Since H3K9me3 localization is usually broad, we consider SICER to be more appropriate than MACS2. For the ChIP analysis in Fig. 3e, ChIP-seq reads obtained from SRA were trimmed using trim\_galore (v.0.5.0) with the --paired setting. Trimmed reads were mapped to the GRCm38 *M. musculus* reference genome with Bowtie2 (v.2.2.4) in paired-end mode using the --very-sensitive setting. ChIP-seq tracks were generated using macs2 (v.2.1.1) callpeak independently from the mapped input and signal reads. Fold-enrichment tracks normalized to input were generated using the bdgcmp tool on the resulting Bedgraph files for input and signal. DeepTools (v.3.0.1) was used to produce the heatmaps with flanking sizes of 5-kb upstream and downstream of the TSS and a bin size of 10 bp.

**Analysis of published RNA-seq data.** For this analysis (Fig. 3f,g), we used previous data<sup>22,71</sup> from the Gene Expression Omnibus (GEO; [GSE45719](#) and [GSE38495](#)). Single-end reads were trimmed for adaptor sequences using trimomatic 0.36 and mapped to the mm10 reference genome using STAR 2.5.3a and the GENCODE M13 annotation. RPKMs were computed through the HTSeq pipeline, and detectable genes were defined as having a median expression in the single-cell expression dataset higher than zero. Plotting was performed using ggplot2.

**Analysis of published ATAC-seq data.** For this analysis (Fig. 3h), ATAC-seq data<sup>26</sup> was downloaded from GEO accession [GSE66390](#). Paired end reads were trimmed for adaptor sequences using trimomatic 0.36 and mapped to the mm10 reference genome using Bowtie2 with the parameters --dovetail -X 2000 --no-discordant --no-mixed. The resulting bam files were filtered for non-uniquely mapping reads using samtools with a MAPQ threshold of 10 and filtered for duplicates using Picard Tools' MarkDuplicates. Finally, mitochondrial reads were removed using samtools and signal tracks were generated using macs2.1.1 with the parameters --SPMR--nomodel --nolambda--shift-100--extsize 200 for the combined reads of all replicates of the same population. Gene coordinates were obtained from Ensembl using Biomart, and the average ATAC-seq signal over the gene body was plotted using deepTools.

**Paternal H3K9me3 enrichment for TEs.** Mapping was done as previously described<sup>12</sup> using the default multi-mapping strategy of bwa mem. TE annotations were downloaded from Repeatmasker ([http://repeatmasker.org/](#), v.mm9 open-3.2.8). For the TE enrichment spectrum (Extended Data Fig. 3a), the genome was partitioned into 10-kb bins. Bins were assigned and sorted by the average paternal H3K9me3 signal in that region. For each bin, we counted the number of TEs of a given type that lie within a particular bin (measured at the TE centre). The resulting vector was then smoothed using a sliding window average of 1,000 bins and normalized by dividing by its mean and subsequently log<sub>2</sub> transformed. Hence, negative values in the enrichment vector indicate depletion of TE copies in regions with a particular H3K9me3 average, while positive values indicate enrichment. P values were calculated using Mann–Whitney U-tests on the distribution of all average paternal H3K9me3 values in the binned non-smoothed genome versus the distribution of values in bins that contained a copy of the given TE class and adjusted using the Bonferroni procedure. Only TEs with adjusted P values of <0.01 are displayed (Extended Data Fig. 3a). Each row in the spectrum plot corresponds to a single type of TE and columns are ordered by increasing H3K9me3 value (for clarity, all bins with a H3K9me3 average equal to 0 were collapsed into a single column by calculating their average TE enrichment value). Rows were ordered by hierarchical clustering using the centroid linkage method. Enrichment meta-profiles for specific examples (Extended Data Fig. 3b) display the trimmed mean paternal H3K9me3 signal (red line; trimmed mean cut-off of 0.05) in a 40-kb window around all copies of a given TE class. For visual reference, meta-profile plots include a random profile (grey line) generated by randomly choosing the same number of genomic regions in the genome as TE copies (maintaining the number of copies per chromosome) and performing the same enrichment analysis on the random set of regions.

**NicE-seq for accessible chromatin analysis of mouse preimplantation embryos.** Zygotes were cultured until the eight-cell stage (72 h post-hCG).

The zona pellucida was removed and ten eight-cell stage samples were fixed in 1% paraformaldehyde and quenched with 50 mM glycine. The NicE-seq library was prepared using a modified protocol<sup>72</sup>. Libraries were made on streptavidin magnetic beads using a NEB Ultra II kit.

**NicE-seq data processing and peak calling.** Adaptor and low-quality sequences were trimmed from paired-end sequencing reads using Trim Galore ([http://www.bioinformatics.babraham.ac.uk/projects/trim\\_galore/](#)) with the following settings: --clip\_R1 4 --clip\_R2 4 --three\_prime\_clip\_R1 4 --three\_prime\_clip\_R2 4. Trimmed read pairs were mapped to the reference genome (mouse: mm10) using Bowtie2 (ref. <sup>55</sup>) with the following arguments: --dovetail --no-unal--no-mixed--no-discordant--very-sensitive-I 0 -X 1000. Furthermore, PCR duplicates and mitochondrial reads were removed using Picard tools and samtools, respectively. Properly aligned read pairs were used for peak calling with MACS2 (ref. <sup>73</sup>) using 'macs2 callpeak -f BAMPE, --nolambda, --nomodel options. The fraction of reads in peaks score was calculated using the deepTools plotEnrichment function<sup>74</sup>. Peaks from the biological replicates were merged together using BedTools<sup>75</sup>. Peaks called from S and L samples were compared using the BedTools and mergepeaks.pl command of Homer. First peaks from all the samples are concatenated. Peaks with at least one base pair overlapping were considered associated and were merged to form a union peak set. Then peaks of individual samples were compared to the union set and were marked as either "unique" or "common". Last, the numbers of unique and common peaks were summarized from all the samples and were used to make Venn diagrams in R. NicE-Seq peaks were annotated using HOMER annotatePeaks.pl. HOMER annotates peaks as promoter (that is, within 2 kb of a known TSS), intergenic, intronic, exon, CpG islands, repetitive elements and other positional categories. Signal tracks were generated using 100-bp bins using deepTools bamCoverage with the following parameters: --of bigwig --normalizeUsing RPKM.

**Statistics and reproducibility.** Statistical tests were performed minding the data distribution and taking into consideration the number of data points available. Details on sample sizes, in addition to the statistical tests conducted, are shown on the corresponding figure legends. The normality of the distributions was tested using the Kolmogorov–Smirnov test. If the data were found not to be normally distributed, nonparametric two-tailed Mann–Whitney U-test was used, otherwise unpaired Student's t-test was used. The experiments throughout the manuscript were successfully reproduced across the indicated number of experiments as reported in the figure legends. For the results shown in Fig. 2c, seven independent experiments with SUV39H1 and nine independent experiments with SUV39H2 were performed. In five out of the seven experiments with SUV39H1, a modest upregulation of KMT activity was observed (as represented by the figure) and never any downregulation. By contrast, in four out of the nine experiments with SUV39H2, a downregulation was observed (as represented by the figure).

**Reporting Summary.** Further information on research design is available in the Nature Research Reporting Summary linked to this article.

## Data availability

Sequencing data generated during this study have been deposited into the GEO under accession codes [GSE126021](#) (single-embryo RNA-seq for *Suv39h1*wt from the two-cell stage to the morula stage), [GSE126185](#) (RNA-seq for pooled *Suv39h1*-overexpressing embryos at the two-cell stage), [GSE126492](#) (RNA-seq for pooled embryos with *Suv39h2* RNAi at the two-cell stage) and [GSE138686](#) (NicE-seq for embryos with *Suv39h2* RNAi at the eight-cell stage). Previously published mouse embryo datasets re-analysed here are available under accession codes [GSE45719](#) and [GSE38495](#) (single-cell RNA-seq), [GSE66390](#) (ATAC-seq) and [GSE98149](#) (H3K9me3 ChIP-seq). All other data supporting the findings of this study are available from the corresponding author upon reasonable request. Source data are provided with this paper.

## Code availability

All next-generation sequencing data were analysed with standard programs and packages, as detailed in the Methods. Code is available upon request.

## References

47. Tsouroula, K. et al. Temporal and spatial uncoupling of DNA double strand break repair pathways within mammalian heterochromatin. *Mol. Cell* **63**, 293–305 (2016).
48. Lehnertz, B. et al. Suv39h-mediated histone H3 lysine 9 methylation directs DNA methylation to major satellite repeats at pericentric heterochromatin. *Curr. Biol.* **13**, 1192–1200 (2003).
49. Torres-Padilla, M. E., Bannister, A. J., Hurd, P. J., Kouzarides, T. & Zernicka-Goetz, M. Dynamic distribution of the replacement histone variant H3.3 in the mouse oocyte and preimplantation embryos. *Int. J. Dev. Biol.* **50**, 455–461 (2006).

50. Jachowicz, J. W., Santenard, A., Bender, A., Muller, J. & Torres-Padilla, M. E. Heterochromatin establishment at pericentromeres depends on nuclear position. *Genes Dev.* **27**, 2427–2432 (2013).
51. Zhou, Q., Jouneau, A., Brochard, V., Adenot, P. & Renard, J. P. Developmental potential of mouse embryos reconstructed from metaphase embryonic stem cell nuclei. *Biol. Reprod.* **65**, 412–419 (2001).
52. Brochard, V. & Liu, Z. in *Nuclear Reprogramming. Methods in Molecular Biology (Methods and Protocols)* Vol. 1222 (eds Beaujean, N. et al.) 1–14 (Humana Press, 2015)..
53. Picelli, S. et al. Smart-seq2 for sensitive full-length transcriptome profiling in single cells. *Nat. Methods* **10**, 1096–1098 (2013).
54. Trapnell, C., Pachter, L. & Salzberg, S. L. TopHat: discovering splice junctions with RNA-seq. *Bioinformatics* **25**, 1105–1111 (2009).
55. Langmead, B. & Salzberg, S. L. Fast gapped-read alignment with Bowtie 2. *Nat. Methods* **9**, 357–359 (2012).
56. Anders, S., Pyl, P. T. & Huber, W. HTSeq—A Python framework to work with high-throughput sequencing data. *Bioinformatics* **31**, 166–169 (2015).
57. Anders, S. & Huber, W. Differential expression analysis for sequence count data. *Genome Biol.* **11**, R106 (2010).
58. Love, M. I., Huber, W. & Anders, S. Moderated estimation of fold change and dispersion for RNA-seq data with DESeq2. *Genome Biol.* **15**, 550 (2014).
59. Benjamini, Y. & Hochberg, Y. Controlling the false discovery rate: a practical and powerful approach to multiple testing. *J. R. Stat. Soc. Ser. B Stat. Methodol.* **57**, 289–300 (1995).
60. Li, H. & Durbin, R. Fast and accurate short read alignment with Burrows–Wheeler transform. *Bioinformatics* **25**, 1754–1760 (2009).
61. Jurka, J. et al. Repbase Update, a database of eukaryotic repetitive elements. *Cytogenet. Genome Res.* **110**, 462–467 (2005).
62. Bolger, A. M., Lohse, M. & Usadel, B. Trimmomatic: a flexible trimmer for Illumina sequence data. *Bioinformatics* **30**, 2114–2120 (2014).
63. Bray, N. L., Pimentel, H., Melsted, P. & Pachter, L. Near-optimal probabilistic RNA-seq quantification. *Nat. Biotechnol.* **34**, 525–527 (2016).
64. McCarthy, D. J., Campbell, K. R., Lun, A. T. & Wills, Q. F. Scater: pre-processing, quality control, normalization and visualization of single-cell RNA-seq data in R. *Bioinformatics* **33**, 1179–1186 (2017).
65. Robinson, M. D., McCarthy, D. J. & Smyth, G. K. edgeR: a Bioconductor package for differential expression analysis of digital gene expression data. *Bioinformatics* **26**, 139–140 (2010).
66. Haghverdi, L., Buettner, F. & Theis, F. J. Diffusion maps for high-dimensional single-cell analysis of differentiation data. *Bioinformatics* **31**, 2989–2998 (2015).
67. Liu, X. et al. Distinct features of H3K4me3 and H3K27me3 chromatin domains in pre-implantation embryos. *Nature* **537**, 558–562 (2016).
68. Brin d'Amour, J. & AL, E. An ultra-low-input native ChIP-seq protocol for genome-wide profiling of rare cell populations. *Nat. Commun.* **6**, 6033 (2015).
69. Neph, S. et al. BEDOPS: high-performance genomic feature operations. *Bioinformatics* **28**, 1919–1920 (2012).
70. Zang, C. et al. A clustering approach for identification of enriched domains from histone modification ChIP-seq data. *Bioinformatics* **25**, 1952–1958 (2009).
71. Ramsköld, D. et al. Full-length mRNA-seq from single-cell levels of RNA and individual circulating tumor cells. *Nat. Biotechnol.* **30**, 777–782 (2012).
72. Ponnaluri, V. K. C. et al. NicE-seq: high resolution open chromatin profiling. *Genome Biol.* **18**, 122 (2017).
73. Zhang, Y. et al. Model-based analysis of ChIP-Seq (MACS). *Genome Biol.* **9**, R137 (2008).
74. Ramirez, F. et al. deepTools2: a next generation web server for deep-sequencing data analysis. *Nucleic Acids Res.* **44**, W160–W165 (2016).
75. Quinlan, A. R. & Hall, I. M. BEDTools: a flexible suite of utilities for comparing genomic features. *Bioinformatics* **26**, 841–842 (2010).

## Acknowledgements

We thank A. J. Bannister for providing the *Suv39h1* cDNA and S. Daujat for providing the H3K64me3 antibody, K. Swist for help with expression of recombinant SUV39H enzymes and analysis of data shown in Fig. 2c, A. J. Bannister and members of the IES for helpful discussions. We thank A. Ettinger for help with the blind counting and microscopy. C.G. and T.J. were supported by funds from the Max Planck Society. A.E. was partially funded through a MENRT fellowship. M.-E.T.-P. acknowledges funding from EpiGeneSys NoE, ERC-Stg ‘NuclearPotency’, EMBO Young Investigator Programme, the Schlumberger Foundation for Research and Education and the Helmholtz Association and by the Deutsche Forschungsgemeinschaft (DFG, German Research Foundation) project-ID 213249687–SFB 1064. N.B. and V.B. were funded through the Laboratoire d’Excellence REVIVE (Investissement d’Avenir, ANR-10-LABX-73) and the INRA animal facilities (IERP, Jouy-en-Josas, France). J.M.V. acknowledges funding from EpiGeneSys NoE and the Max Planck Society and S.G. from the Ministry of Science and Technology of China (grant number 2016YFA0100400).

## Author contributions

A.B. and M.-E.T.-P. conceived the project and wrote the manuscript. A.B., V.B., C.G., H.G.C. and A.E. performed and designed experiments with the supervision of N.B., T.J., S.P. and M.-E.T.-P. E.R.R.-M., Q.R., D.R.-T., K.K., S.L.G., V.S.U., X.L. and C.W. performed and designed computational analysis with the supervision of S.G., S.P., J.M.V. and M.-E.T.-P.

## Competing interests

The authors declare no competing interests.

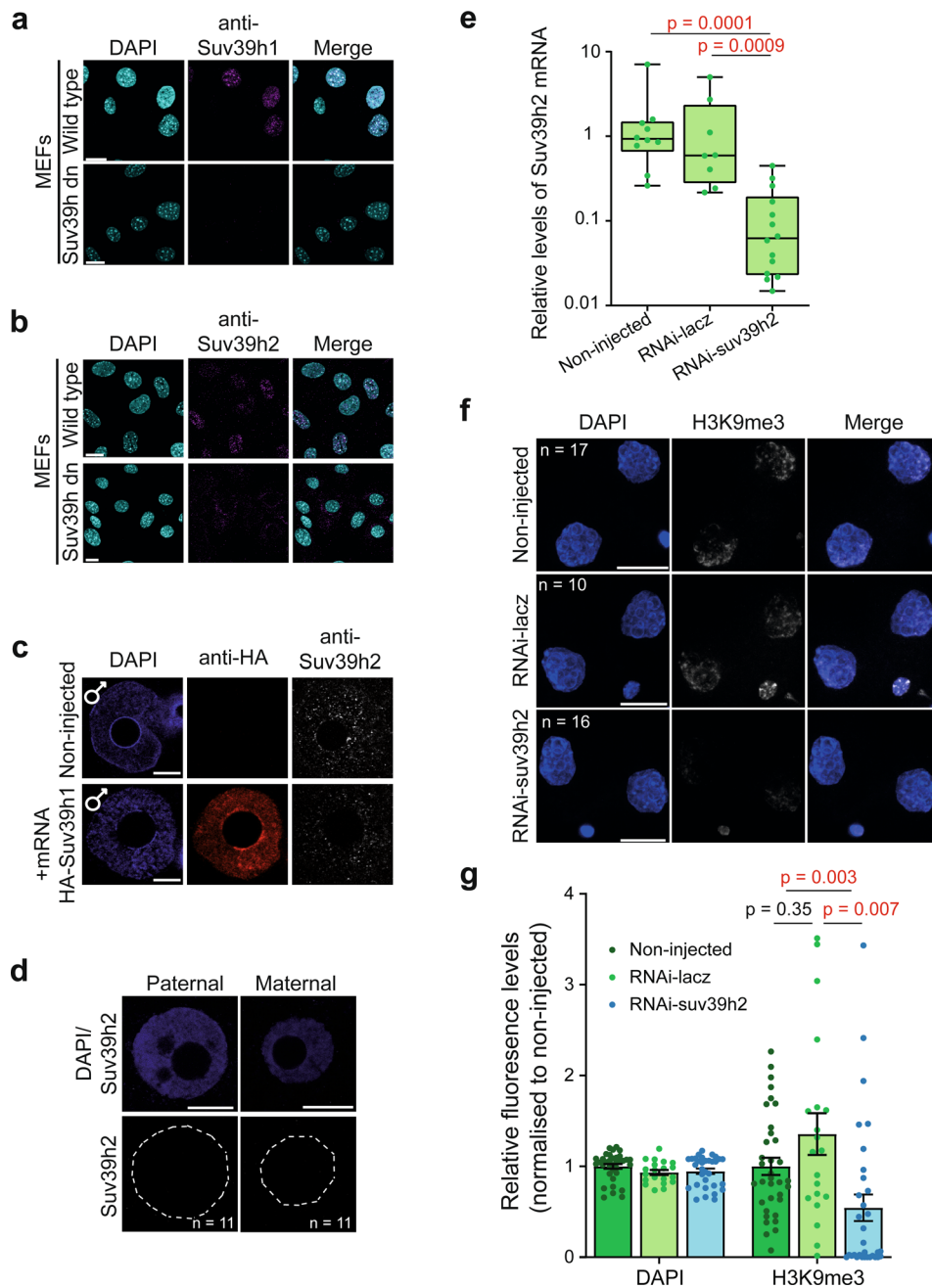
## Additional information

**Extended data** is available for this paper at <https://doi.org/10.1038/s41556-020-0536-6>.

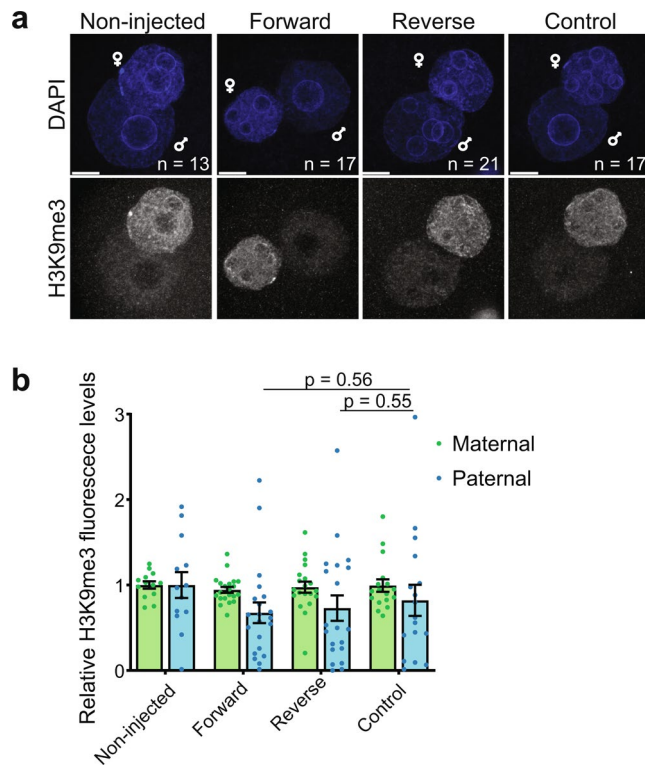
**Supplementary information** is available for this paper at <https://doi.org/10.1038/s41556-020-0536-6>.

**Correspondence and requests for materials** should be addressed to M.-E.T.-P.

**Reprints and permissions information** is available at [www.nature.com/reprints](http://www.nature.com/reprints).

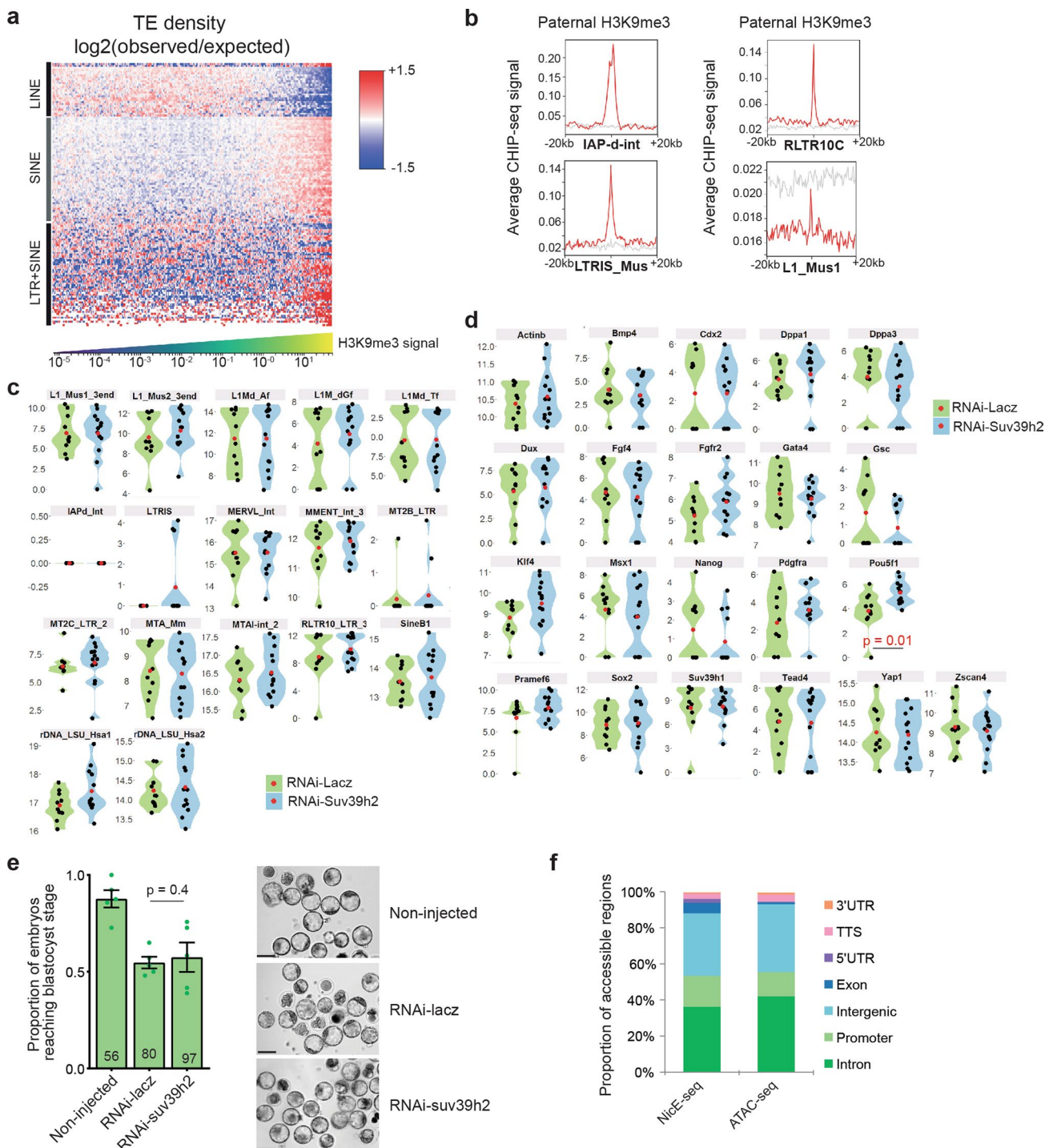


**Extended Data Fig. 1 | De novo H3K9me3 activity occurs immediately after fertilization.** **a, b.** Wild-type and *Suv39h1/2* double knock-out MEF cells immunostained with a anti-SUV39H1 and b anti-SUV39H2 antibody. Shown is a representative single confocal section from 2 independent experiments. Scale bar 20  $\mu$ m. **c.** Zygotes microinjected with HA-Suv39h1 mRNA as described in Fig. 4a were fixed and immunostained with anti-HA and anti-SUV39H2 antibodies after 8 h. A representative single confocal section of the paternal pronucleus in 7 zygotes from 2 independent experiments is shown. The anti-SUV39H2 antibody does not recognise SUV39H1 protein. Scale bar 10  $\mu$ m. **d.** SUV39H2 immunostaining in the two pronuclei in the early zygote (19 h post-hCG). Shown is a representative embryo of 11 from 3 independent experiments. **e.** Knockdown efficiency of dsRNA targeting *Suv39h2* was assessed by RT-qPCR of *Suv39h2* mRNA at 30 h post-hCG in single embryos, the same timing as the immunofluorescence experiments shown in Fig. 1g, h. The data represents the average fold change of *Suv39h2* levels normalized to average levels of *Actin-b* and *Gapdh* in each embryo. N = the indicated number of embryos across 3 independent experiments. The box plots depict the median and interquartile range. The two sided Mann-Whitney U-test was used to compare experimental groups. **f.** Representative maximum intensity projections of 2-cell stage embryos upon *Suv39h2* RNAi using dsRNA, immunostained with anti-H3K9me3 antibodies. N = total number of individual embryos analysed in each group across 3 independent experiments for *Suv39h2* and 2 for control knockdown. Scale bar 10  $\mu$ m. **g.** Quantification of average fluorescence intensity for H3K9me3 in 2-cell stage nuclei. Data were normalized to the average H3K9me3 signal in non-injected embryos and are presented as mean  $\pm$  S.E.M (n = as in f). Statistical analysis was performed using the two-sided Mann-Whitney U test for comparing nonparametric distributions. Statistical source data are shown in Source Data Fig. 1.

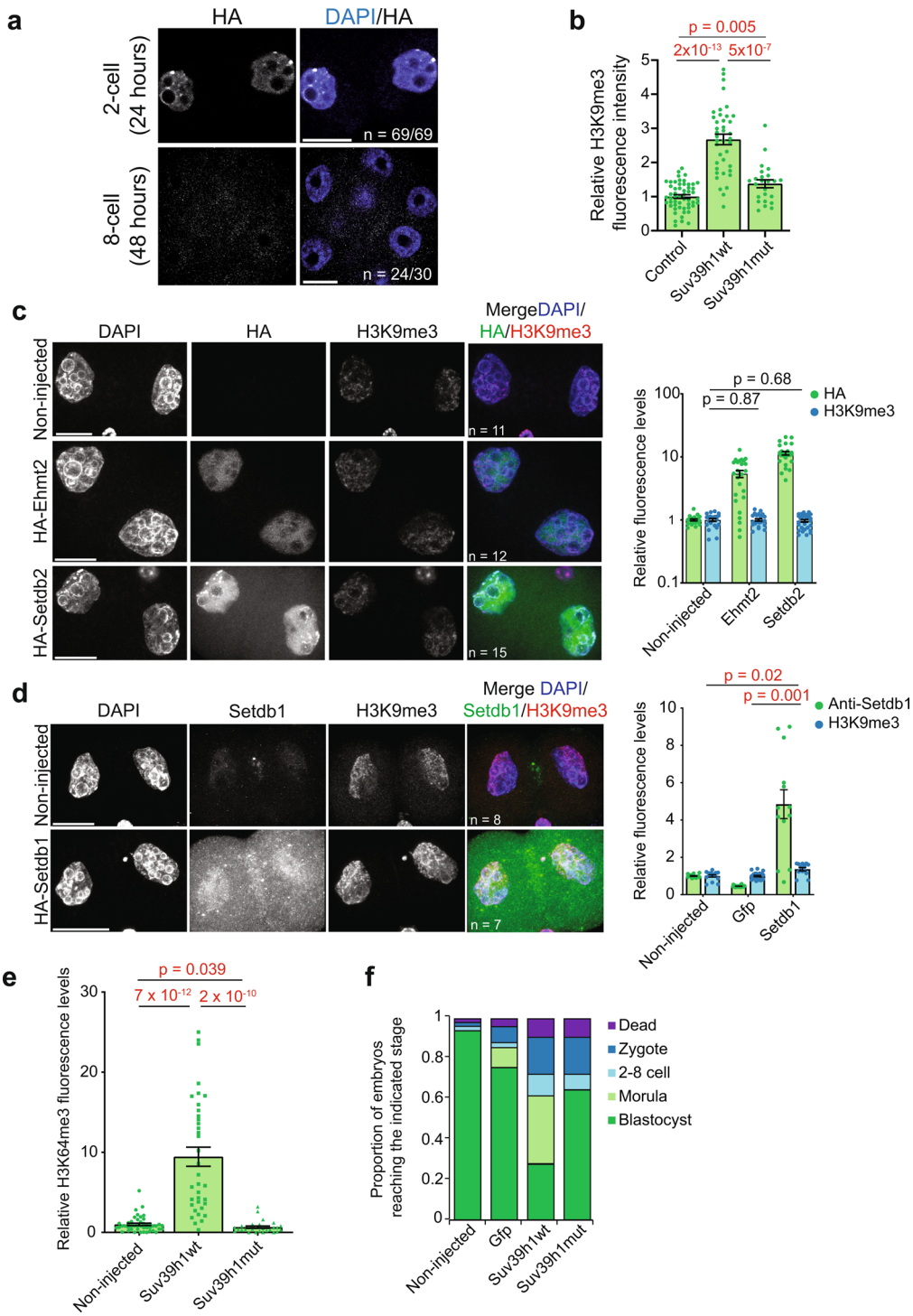


**Extended Data Fig. 2 | RNA modulation of the KMT activity of SUV39H2 attenuates H3K9me3 levels in the early preimplantation mouse embryo.**

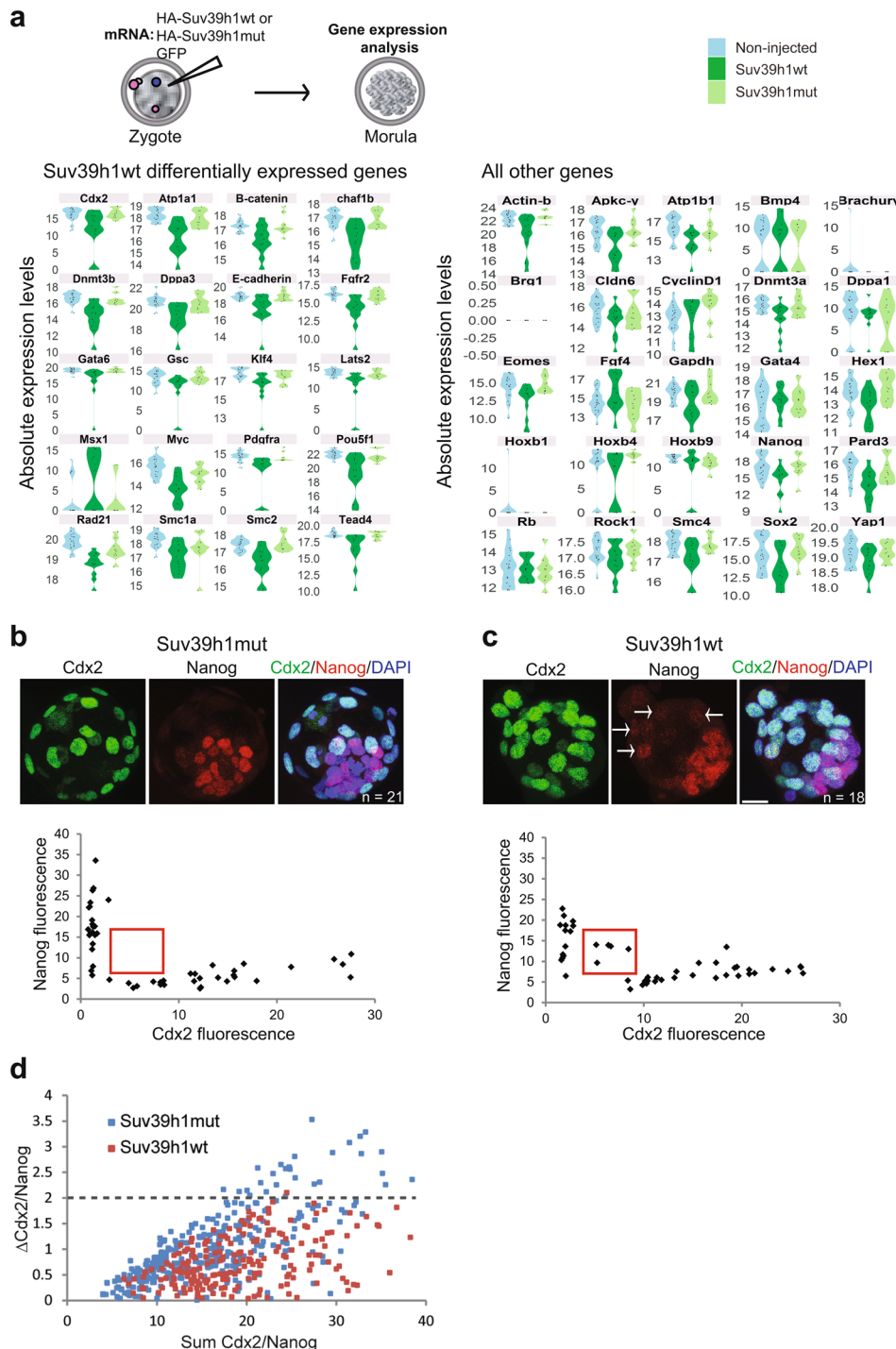
**a.** Representative full z-series projections of confocal stacks of the indicated number of embryos manipulated as described in Fig. 2d, injected instead with single-stranded forward or reverse major satellite transcripts from 2 independent experiments. Paternal and maternal pronuclei are indicated. Scale bar 10  $\mu$ m. **b.** Quantification of the levels of H3K9me3 staining in the maternal and paternal pronuclei across embryos represented in a. Maternal and paternal H3K9me3 levels were normalized to average levels in non-injected embryo. The graph depicts the mean  $\pm$  S.E.M. (n = the number of embryos analysed as indicated in a across 2 independent experiments). Statistical analysis was performed using the two-sided Mann-Whitney U test for comparing nonparametric distributions. Statistical source data are shown in Source Data Extended Data Fig. 2.



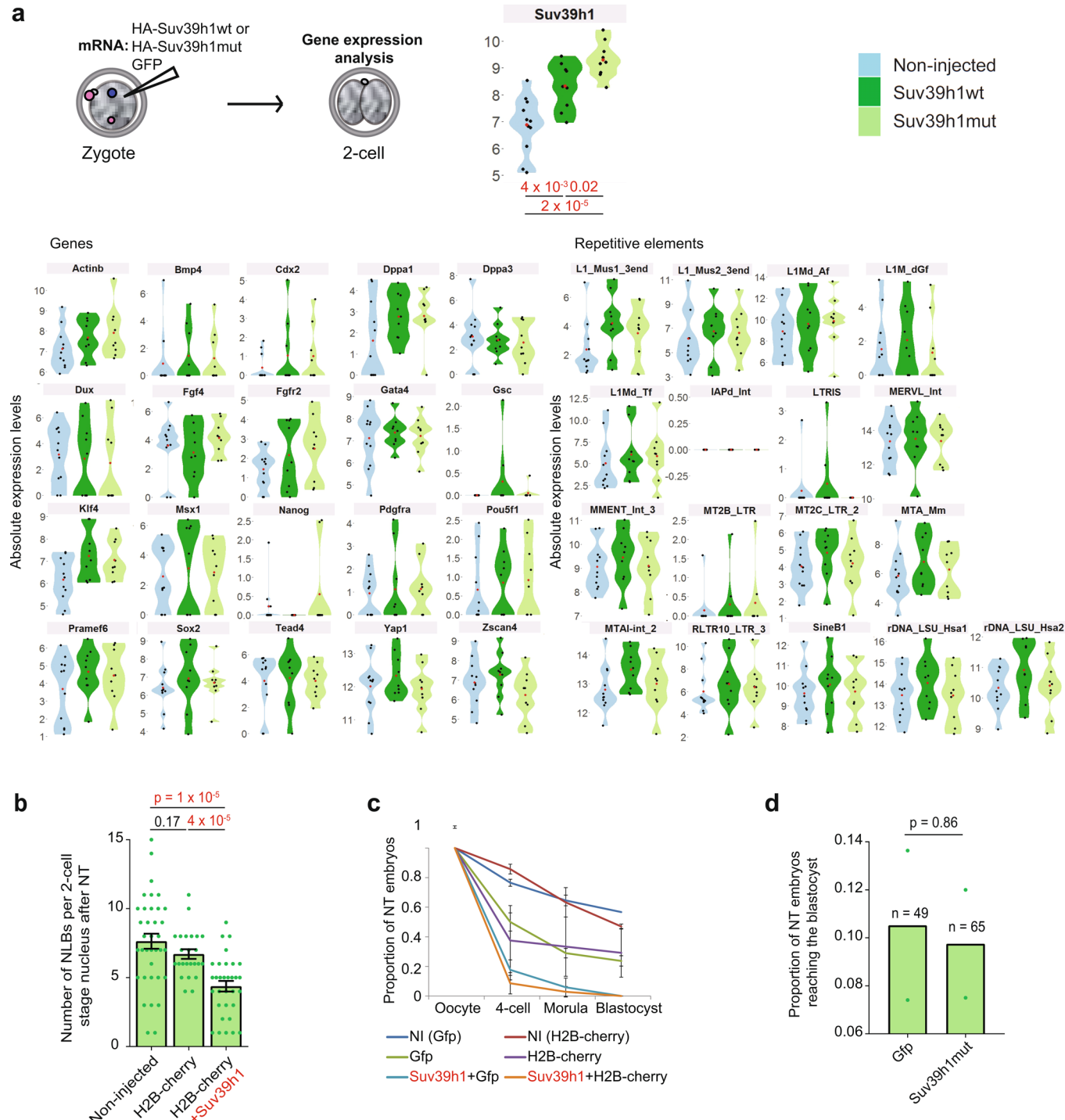
**Extended Data Fig. 3 | H3K9me3 is compatible with gene expression during early preimplantation development.** **a.** Enrichment heatmap ( $\log_2$  observed/expected TE density) in regions with differing paternal H3K9me3 levels. Columns correspond to 10 kb binned genomic regions sorted from left to right by increasing H3K9me3 levels. Rows correspond to individual TE types hierarchically clustered using the centroid linkage method. Clusters are coarsely annotated with the dominant TE families. H3K9me3 ChIPseq data from<sup>12</sup> was reanalyzed for panels **a** and **b**. **b.** Examples of paternal H3K9me3 levels in a 40 kb region around selected TE classes (red line, 5% trimmed mean; grey, randomized signal). **c-d.** Violin plots showing relative expression values of the indicated repetitive elements (**c**) or genes (**d**) in knockdown of *Suv39h2* against control (*LacZ*) knockdown embryos at the 2-cell stage (46 h post-hCG). The mean expression value of  $n=10$  embryos (control) and  $n=13$  embryos (*Suv39h2* knockdown) from 3 independent experiments is depicted as a red point and the individual expression in each embryo as black dots. Statistical analysis was performed using the two-sided Mann-Whitney U test. See Supplementary Table 4 for a list of genes (sheet1), REs (sheet2), and for the genes Taqman® assay IDs and reason(s) for inclusion. **e.** Shown is the mean ( $\pm$  S.E.M.) proportion of embryos that reached the blastocyst stage 3 days after microinjection ( $n$ =the total number of embryos analysed is indicated from 5 independent experiments). Statistical analysis was performed using the N-1 Chi-squared test for comparing independent proportions. On the right are shown representative brightfield images of embryos. Images were taken at 120 h post-hCG injection. Scale bar 100  $\mu$ m. **f.** Comparison of the genomic distribution of open chromatin identified by NicE-seq compared to ATAC-seq in 8-cell stage mouse preimplantation embryos. Statistical source data are shown in Source Data Extended Data Fig. 3.



**Extended Data Fig. 4 | SUV39H1 induces constitutive heterochromatin.** **a.** Zygotes were microinjected with HA-Suv39h1 mRNA, cultured for 24 or 48 h, fixed and immunostained with an anti-HA antibody. A representative full z-series projection from at least 3 independent experiments is shown. Scale bar 10  $\mu$ m. **b.** Mean levels of H3K9me3 ( $\pm$ S.E.M) in 2-cell embryos (42–44 h post-hCG). Confocal stacks were reconstructed with IMARIS and nuclei were segmented using the DAPI channel. Fluorescence intensity was quantified in each nucleus after background subtraction. N = numbers as in Fig. 4d. Statistical analysis was performed using the two-sided Mann-Whitney U test. **c.** Zygotes were microinjected with Ehmt2 (G9a) or Setdb2 mRNA, fixed at the 2-cell stage (42–44 h post-hCG) and immunostained with anti-H3K9me3 and anti-HA antibodies. A representative full z-series projection is shown. Mean fluorescence levels ( $\pm$  S.E.M.) are shown on the right (n = the total number of embryos analysed as indicated on the left panels across 2 independent experiments). Statistical analysis was performed using the Mann-Whitney U test. Scale bar 20  $\mu$ m. **d.** As in c but with Setdb1 mRNA. Mean fluorescence levels ( $\pm$  S.E.M.) are shown on the right (n = the total number of embryos analysed as indicated on the left panels across 2 independent experiments). Statistical analysis was performed using the two-sided T test. Scale bar 20  $\mu$ m. **e.** Mean levels ( $\pm$  S.E.M) of H3K64me3 in 2-cell stage embryos (42–44 h post-hCG injection) after Suv39h1wt or Suv39h1mut expression. N = total number of embryos analysed is show in Fig. 4h across 5 independent experiments for Suv39h1wt and 4 for Suv39h1mut. Statistical analysis was performed using the two-sided Mann-Whitney U test. **f.** Summary of the stages of development for which embryos arrested as described in Fig. 5b. N = numbers as in Fig. 5b. Statistical source data are shown in Source Data Extended Data Fig. 4.



**Extended Data Fig. 5 | SUV39H1 compromises development.** **a.** Violin plots depicting absolute expression levels (log<sub>2</sub> scale) in single *Suv39h1wt*, *Suv39h1mut*-expressing embryos and non-injected controls at the morula stage (78 h post-hCG). Expression values in individual embryos are indicated by black points and the mean by a red point. Genes with a significant difference ( $P < 0.05$ ; two-sided Mann-Whitney U test) between the *Suv39h1wt* group and both control groups are shown on the left. N = numbers and stages of the embryos acquired from 3 independent experiments are shown in Supplementary Table 5 and a list of genes analysed are shown in Supplementary Table 6. **b, c.** Embryos injected with mRNA encoding *Suv39h1mut* (control) or (**c**) *Suv39h1wt* were cultured to the blastocyst stage, fixed and immunostained with the indicated antibodies. Shown are representative full z-series projections. N = number of embryos analyzed from 2 independent experiments is indicated. Scale bar 20  $\mu\text{m}$ . Arrows in Nanog panel in **c** indicate cells ectopically expressing low levels of NANOG. The graphs below show the levels of NANOG and CDX2 in individual nuclei, for the representative embryos above. A clear segregation of CDX2 or NANOG positive populations is apparent in the controls, but is less pronounced in the *Suv39h1wt*-injected embryos. The red box indicates a consistent population of double CDX2/NANOG positive cells present in *Suv39h1wt* embryos only. **d.** The absolute difference in intensity ( $\Delta \text{CDX2/NANOG}$ ) for each nucleus (plotted points) from the embryos classified as blastocysts (>32 cells) plotted against the sum of the NANOG and CDX2 signal (n = 7 embryos for *Suv39h1mut* and 5 for *Suv39h1wt* across 2 independent experiments). Fewer nuclei have high  $\Delta \text{CDX2/NANOG}$  and more nuclei have high sum CDX2/NANOG scores in the *Suv39h1wt* embryos, suggesting a defect in the resolution of the outer and inner lineages. Statistical source data are shown in Source Data Extended Data Fig. 5.



**Extended Data Fig. 6 | SUV39H1 inhibits epigenetic reprogramming.** **a.** Violin plots depicting absolute expression levels in log<sub>2</sub> scale in single *Suv39h1wt*, *Suv39h1mut*-expressing embryos and non-injected controls at the late 2-cell stage (46 h post-hCG). N = 9, 9 and 11 single embryos respectively across 3 independent experiments. Expression values in individual embryos are indicated by black points and the mean by a red point. The only gene or RE displaying significant difference using the two-sided Mann-Whitney U test between groups is *Suv39h1* itself. See Supplementary Table 4 for a list of genes (sheet1), REs (sheet2), and for the genes Taqman® assay IDs and reason(s) for inclusion. **b.** The mean number of nucleolar-like bodies (NLBs) ( $\pm$  S.E.M.) inside each 2-cell stage nucleus from confocal stacks of DAPI stained embryos was counted manually (n = the number of embryos analysed is indicated across 4 independent experiments). Nuclear transfer embryos were fixed at 25 and 33 h post-activation with similar results obtained at the two time points. Statistical testing was performed using the two-sided Mann-Whitney U test for comparing nonparametric distributions. **c.** Shown is a summary of the developmental progression of nuclear transfer embryos microinjected with the indicated mRNAs according to the workflow in Fig. 7a. Developmental progression was monitored daily and the proportion of embryos that reached each stage of development was calculated. The data represents the mean ( $\pm$  S.E.M.) (n = the total number of embryos analysed as indicated in Fig. 7c across 3 independent experiments except for H2B-cherry alone, which was done twice). **d.** The mean proportion of embryos injected with *Suv39h1mut* or *Gfp*mRNA developing to the blastocyst stage is shown. N = the number of embryos tested across 2 independent experiments is indicated on the graph. Statistical analysis was performed using the N-1 Chi-squared test for comparing independent proportions. Statistical source data are shown in Source Data Extended Data Fig. 6.

# Reporting Summary

Nature Research wishes to improve the reproducibility of the work that we publish. This form provides structure for consistency and transparency in reporting. For further information on Nature Research policies, see [Authors & Referees](#) and the [Editorial Policy Checklist](#).

## Statistics

For all statistical analyses, confirm that the following items are present in the figure legend, table legend, main text, or Methods section.

n/a Confirmed

- The exact sample size ( $n$ ) for each experimental group/condition, given as a discrete number and unit of measurement
- A statement on whether measurements were taken from distinct samples or whether the same sample was measured repeatedly
- The statistical test(s) used AND whether they are one- or two-sided  
*Only common tests should be described solely by name; describe more complex techniques in the Methods section.*
- A description of all covariates tested
- A description of any assumptions or corrections, such as tests of normality and adjustment for multiple comparisons
- A full description of the statistical parameters including central tendency (e.g. means) or other basic estimates (e.g. regression coefficient) AND variation (e.g. standard deviation) or associated estimates of uncertainty (e.g. confidence intervals)
- For null hypothesis testing, the test statistic (e.g.  $F$ ,  $t$ ,  $r$ ) with confidence intervals, effect sizes, degrees of freedom and  $P$  value noted  
*Give P values as exact values whenever suitable.*
- For Bayesian analysis, information on the choice of priors and Markov chain Monte Carlo settings
- For hierarchical and complex designs, identification of the appropriate level for tests and full reporting of outcomes
- Estimates of effect sizes (e.g. Cohen's  $d$ , Pearson's  $r$ ), indicating how they were calculated

*Our web collection on [statistics for biologists](#) contains articles on many of the points above.*

## Software and code

Policy information about [availability of computer code](#)

Data collection

LAS AF X (version 2.0) was used for imaging data acquisition and basic image manipulation. Imaris versions 7.7 and 8.3 were used for 3D reconstruction of embryos and quantification of fluorescence intensity.

Data analysis

GraphPad Prism (version 8.1.0), Microsoft excel (10) and RStudio (version 1.0.136) were used for data analysis. Custom code generated to perform the analysis in this study is available upon request. Adobe Creative Suite was used for Figure preparation: Illustrator version 16.0.3, Photoshop version 13.01. The R programming language (versions R-3.1.2, R-3.4.0 and R-3.4.3) (<https://www.R-project.org/>) was widely used within the study for statistical analysis and data plotting, all custom code is available on request. Basecalling and filtering were performed using standard software of the Illumina HiSeq 2500 (<https://www.illumina.com/systems/sequencing-platforms/hiseq-2500.html>). Tophat v2.0.14 52 and bowtie v2-2.1.0 were used for mapping 2-cell stage (Suv39h1) RNAseq data. BWA v0.6.2 was used for repeat analysis. For Suv39h2 k.d. data BBduk was used to trim reads. STAR (version 2.5.2b) was used for mapping. HTSeq tool htseq-count (version 0.9.1) was used for read counting against the gene annotations downloaded from gencode (Release M12, GRCm38.p5) with reverse strand setting. For single embryo RNAseq Trimmomatic v0.38 and Kallisto v0.44.0 were used for read cleaning and alignmnet respectively. Quality control tests were carried out using the R packages Scater (v 3.10). Counts were normalised using edgeR (v 3.10). DESeq2 (versions 1.14.1, 1.18.1, and 1.22.1) was used throughout for differential expression analysis. ggplot2 was used for visualization purposes. For ChIP-seq analysis BEDOPS' bedmap v( 2.4.38) was used to calculate enrichments. SICER (v1) was used to generate metagene plots. Macs2 (version 2.1.1) trim\_galore (v0.5.0) was used fro trimming.was used for peak finding. For analysis of published RNA-seq data trimmomatic v0.36 and STAR v2.5.3a were used. For analysis of ATAC-seq data bowtie2 v2-2.1.0 and macs2.1.1 were used for mapping. DeepTools (version 3.0.1) was used to generate heatmaps for both ChIP-seq and ATAC-seq data. For Nice-seq analysis trim\_galore (v0.5.0) and bowtie (v2-2.1.0), Bedtools (v 2.29) Macs2 (v 2.1.1) and HOMER (v4.10) were used.

For manuscripts utilizing custom algorithms or software that are central to the research but not yet described in published literature, software must be made available to editors/reviewers. We strongly encourage code deposition in a community repository (e.g. GitHub). See the Nature Research [guidelines for submitting code & software](#) for further information.

## Data

Policy information about [availability of data](#)

All manuscripts must include a [data availability statement](#). This statement should provide the following information, where applicable:

- Accession codes, unique identifiers, or web links for publicly available datasets
- A list of figures that have associated raw data
- A description of any restrictions on data availability

Sequencing data generated during this study have been deposited in the Gene Expression Omnibus (GEO) under accession codes GSE126021 (single-embryo RNA-seq for Suv39h1wt from 2-cell to morula stage); GSE126185 (RNA-seq for pooled Suv39h1-overexpressing embryos at 2-cell stage); GSE126492 (RNA-seq for pooled embryos with RNAi-Suv39h2 at 2-cell stage), GSE138686 (NicE-seq for embryos with RNAi-Suv39h2 at 8-cell stage).

Previously published mouse embryo datasets re-analysed here are available under accession codes GSE45719 and GSE38495 (single cell RNA-Seq); GSE66390 (ATACseq) and GSE98149 (H3K9me3 ChIP-seq).

Figures with associated raw data are as follows: Fig. 1c, 1h, 2f, 2h, 4f, 5b, 5e, 5f, 7c, 7d, Extended Data Fig. 1e, 1g, 2b, 3e, 4b, 4c, 4d, 4e, 4f, 5d, 6b, 6c, 6d

## Field-specific reporting

Please select the one below that is the best fit for your research. If you are not sure, read the appropriate sections before making your selection.

Life sciences       Behavioural & social sciences       Ecological, evolutionary & environmental sciences

For a reference copy of the document with all sections, see [nature.com/documents/nr-reporting-summary-flat.pdf](http://nature.com/documents/nr-reporting-summary-flat.pdf)

## Life sciences study design

All studies must disclose on these points even when the disclosure is negative.

Sample size At least 3 biological replicates were included (unless otherwise stated) based on previously published work and preliminary studies as standard for this field of research. See Figures legends for each experiment.

Data exclusions No data were excluded.

Replication All attempts at replication were successful as reported in the manuscript with the exception of Figure 2c (see below). Variability in the data is reported with the use of error bars representing standard error of the mean (S.E.M.) throughout the manuscript. Statistical analysis (Mann-Whitney U test for non-parametric data or students t test for parametric data) was applied to biologically independent samples to assess the probability of obtaining the results by chance and reported as p values in all Figures. The number of experimental replicates are stated in the legends throughout. For Figure 2c seven independent experiments with Suv39h1 and nine independent experiments with Suv39h2 were performed. In 5 out of the 7 experiments with Suv39h1, a modest upregulation of KMT activity (as represented by the Figure) was observed and never any downregulation. By contrast, in 4 out of the 9 experiments with Suv39h2, a downregulation was observed (as represented by the Figure and stated in the legend).

Randomization Embryos were allocated at random to experimental groups as stated in the Methods

Blinding Blind counting was carried out for Figure 4f-g in which relatively subjective counting was performed. All other analysis was objectively performed using automated approaches. Experimentors were not blinded during group allocation, embryos were divided randomly between groups.

## Reporting for specific materials, systems and methods

We require information from authors about some types of materials, experimental systems and methods used in many studies. Here, indicate whether each material, system or method listed is relevant to your study. If you are not sure if a list item applies to your research, read the appropriate section before selecting a response.

### Materials & experimental systems

n/a	Involved in the study
<input type="checkbox"/>	<input checked="" type="checkbox"/> Antibodies
<input type="checkbox"/>	<input checked="" type="checkbox"/> Eukaryotic cell lines
<input checked="" type="checkbox"/>	<input type="checkbox"/> Palaeontology
<input type="checkbox"/>	<input checked="" type="checkbox"/> Animals and other organisms
<input checked="" type="checkbox"/>	<input type="checkbox"/> Human research participants
<input checked="" type="checkbox"/>	<input type="checkbox"/> Clinical data

### Methods

n/a	Involved in the study
<input checked="" type="checkbox"/>	<input type="checkbox"/> ChIP-seq
<input checked="" type="checkbox"/>	<input type="checkbox"/> Flow cytometry
<input checked="" type="checkbox"/>	<input type="checkbox"/> MRI-based neuroimaging

## Antibodies

### Antibodies used

Antibodies used were as follows: (dilutions): anti-Suv39h1 (Cell Signalling 8729), anti-Suv39h2 (Abcam 104343) (1:100), anti-HA (Roche 11867423001), anti-H3K9me3 (Millipore 07-442), anti-H3K9me3 (Active Motif 39286) (1:100) (used only in relation to Fig 1), anti-H4K20me3 (Millipore 07-463), anti-H3K64me3 (generous gift from S. Daujat IGBMC, France), anti-GFP (Abcam ab13970) (1:1000), anti-CenpA/B (Europa Bioproducts F290C-CS1058) (1:500), anti-Cdx2 (BioGenex AM392-5M) (1:500), anti-Nanog (CosmoBio RCAB0002P-F) (1:500), and anti-Oct4 (BD Bioscience 611203). Dilutions were 1:250 unless otherwise indicated. Secondary antibodies used were A32731, A32732, A32733, A10522, A-11029, A-21424, A32728, A-21445, 1:500 dilution.

### Validation

Anti-Suv39h1 and Suv39h2 antibodies were validated by immunofluorescence against Suv39h1/2 mouse knockout cell lines (Extended Data Figure 1a-b). Two different antibodies against H3K9me3 (Millipore 07-442, Active Motif 39286) were used with similar results regarding Figure 1g-h. Anti-H3K9me3 (Millipore 07-442) was validated by blot blot and the manufacturer ([https://www.merckmillipore.com/DE/de/product/Anti-trimethyl-Histone-H3-Lys9-Antibody,MM\\_NF-07-442](https://www.merckmillipore.com/DE/de/product/Anti-trimethyl-Histone-H3-Lys9-Antibody,MM_NF-07-442)). Active motif anti-H3K9me3 was validated by the manufacturer (<https://www.activemotif.com/catalog/details/39285/histone-h3-trimethyl-lys9 antibody-mab-clone-2ag-6f12-h4>). HA-tag antibody was validated by the manufacturer (<https://www.sigmaaldrich.com/catalog/product/roche/roahaha?lang=de&region=DE>). Anti-H4K20me3 was validated by the manufacturer ([https://www.merckmillipore.com/DE/de/product/Anti-trimethyl-Histone-H4-Lys20-Antibody,MM\\_NF-07-463?ReferrerURL=https%3A%2F%2Fwww.google.com%2F&bd=1](https://www.merckmillipore.com/DE/de/product/Anti-trimethyl-Histone-H4-Lys20-Antibody,MM_NF-07-463?ReferrerURL=https%3A%2F%2Fwww.google.com%2F&bd=1)). Anti-H3K64me3 was validated in Daujat et al., Nat Struct Mol Biol. 2009. Anti-GFP was validated by the manufacturer (<https://www.abcam.com/gfp-antibody-ab13970.html>). Anti-CenpA/B was validated by the manufacturer. Anti-Cdx2 was validated by the manufacturer (<http://store.biogenex.com/us/applications/ihc/controls/controls/anti-cdx-2-clone-cdx2-88.html>). Anti-Nanog was validated by the manufacturer (<https://www.cosmobiousa.com/products/anti-nanog-mouse-pab>). Anti-Oct3/4 was validated by the manufacturer (<https://www.bdbiosciences.com/eu/applications/research/stem-cell-research/cancer-research/human/purified-mouse-anti-oct-34-40oct-3/p/611203>).

## Eukaryotic cell lines

### Policy information about [cell lines](#)

#### Cell line source(s)

Suv39h1/2 double knock-out MEF cells originating from Suv39h1/2 knockout mice (Peters et al., Cell 2001).

#### Authentication

The Suv39h1/2 double knock-out MEF cells have previously been characterised in Peters et al., Cell 2001.

#### Mycoplasma contamination

All cell lines tested negative for mycoplasma contamination.

#### Commonly misidentified lines (See [ICLAC](#) register)

No commercially misidentified cell lines were used.

## Animals and other organisms

### Policy information about [studies involving animals; ARRIVE guidelines](#) recommended for reporting animal research

#### Laboratory animals

F1 (C57BL6 X CBA/H) mice were used to provide oocytes and crossed with F1 males to provide zygotes. For ChipSeq B6D2F1 female mice were mated with C57BL6 males. DBA/2 males were crossed with F1 females for Nice-Seq.

#### Wild animals

This study did not use wild animals.

#### Field-collected samples

This study did not involve field-collected samples.

#### Ethics oversight

All experiments were approved by the Ethics Committee of the Université de Strasbourg and performed under the authorization of French legislation or of the Upper Bavarian authorities. For nuclear transfer N.B. has the authorization to work with laboratory animals from the departmental veterinary regulatory service (license N° 78–95) and from the local ethics committee (N° 12/123 - Comethea Jouy-en-Josas/AgroParisTech).

Note that full information on the approval of the study protocol must also be provided in the manuscript.